Atmos. Chem. Phys. Discuss., 12, 25121–25180, 2012
www.atmos-chem-phys-discuss.net/12/25121/2012/
doi:10.5194/acpd-12-25121-2012

Atmospheric Chemistry and Physics Discussions

Black carbon physical properties and mixing state in the European megacity Paris

M. Laborde[1], M. Crippa[1], T. Tritscher[1,*], Z. Jurányi[1,], P. F. DeCarlo[1,***], B. Temime-Roussel[2], N. Marchand[2], S. Eckhardt[3], A. Stohl[3], U. Baltensperger[1], A. S. H. Prévôt[1], E. Weingartner[1], and M. Gysel[1]**

[1]Laboratory of Atmospheric Chemistry, Paul Scherrer Institute, Villigen PSI, Switzerland
[2]Aix-Marseille Université, Laboratoire Chimie Environnement, Marseille, France
[3]NILU – Norwegian Institute for Air Research, Kjeller, Norway
[*]now at: TSI GmbH, Particle Instruments, Aachen, Germany
[**]now at: Institute of Aerosol and Sensor Technology, University of Applied Sciences Northwestern Switzerland, Windisch, Switzerland
[***]now at: Department of Civil, Architectural, and Environmental Engineering, Drexel University, Philadelphia, PA, USA

Received: 9 August 2012 – Accepted: 31 August 2012 – Published: 24 September 2012

Correspondence to: M. Gysel (martin.gysel@psi.ch)

Published by Copernicus Publications on behalf of the European Geosciences Union.

Abstract

Aerosol hygroscopicity and black carbon (BC) properties were characterised during wintertime in Paris, one of the biggest European megacities. Hygroscopic growth factor (GF) distributions, characterised by distinct modes of more-hygroscopic background aerosol and non- or slightly hygroscopic aerosol of local (or regional) origin, revealed an increase of the relative contribution of the local sources compared to the background aerosol with decreasing particle size. BC particles in Paris were mainly originating from fresh traffic emissions, whereas biomass burning was only a minor contribution. The mass size distribution of the BC cores peaked on average at a BC core mass equivalent diameter of $D_{\mathrm{MEV}} \approx 150$ nm. The BC particles were moderately coated ($\Delta_{\mathrm{coat}} \approx 30$ nm on average for BC cores with $D_{\mathrm{MEV}} = 160$–260 nm) and an average mass absorption coefficient (MAC) of $\sim 8.6\ \mathrm{m^2\,g^{-1}}$ at the wavelength $\lambda = 880$ nm was observed.

Different time periods were selected to investigate the properties of BC particles as a function of source and air mass type. The traffic emissions were found to be non-hygroscopic (GF ≈ 1.0), and essentially all particles with a dry mobility diameter larger than $D_0 = 110$ nm contained a BC core. BC from traffic emissions was further characterised by literally no coating ($\Delta_{\mathrm{coat}} \approx 2$ nm), the smallest maximum of the BC core mass size distribution ($D_{\mathrm{MEV}} \approx 100$ nm) and the smallest MAC ($\sim 7.3\ \mathrm{m^2\,g^{-1}}$ at $\lambda = 880$ nm).

The biomass burning aerosol was slightly more-hygroscopic than the traffic emissions (with a distinct slightly hygroscopic mode peaking at GF ≈ 1.1–1.2). Furthermore, only a minor fraction ($\lesssim 10\,\%$) of the slightly hygroscopic particles with GF $\gtrsim 1.1$ (and $D_0 = 265$ nm) contained a detectable BC core. The BC particles from biomass burning were found to have a medium coating thickness as well as slightly larger mean BC core sizes and MAC values compared to traffic emissions.

The aerosol observed under the influence of aged air masses and air masses from Eastern Continental Europe was dominated by a more-hygroscopic mode peaking at GF ≈ 1.6. Most particles (95 %) with a $D_0 = 265$ nm, in this mode, did not contain

Title Page
Abstract | Introduction
Conclusions | References
Tables | Figures
◀| |▶
◀ ▶
Back | Close
Full Screen / Esc
Printer-friendly Version
Interactive Discussion

a boxdetectable BC core. A significant fraction of the BC particles had a substantial coating with non-refractory aerosol components. MAC values of $\sim 8.8\,\mathrm{m^2\,g^{-1}}$ and $\sim 8.3\,\mathrm{m^2\,g^{-1}}$ at $\lambda = 880\,\mathrm{nm}$ and mass mean BC core diameters of 150 nm and 200 nm were observed for the aged and continental air mass types, respectively. The reason for the larger BC core sizes compared to the fresh emissions – transport effects or a different BC source – remains unclear.

The dominant fraction of the BC-containing particles was found to have no or very little coating with non-refractory matter. The lack of coatings is consistent with the observation that the BC particles are non- or slightly hygroscopic, which makes them poor cloud condensation nuclei.

1 Introduction

Particles emitted during incomplete combustion of biofuel, fossil fuel and open biomass burning are composed of different amounts of black carbon (BC), primary organic matter (POM) and inorganic salts depending on the sources. Atmospheric BC strongly absorbs sunlight at all wavelengths warming up the surrounding air and therefore the climate (Jacobson, 2001; Chung and Seinfeld, 2002; Ramanathan and Carmichael, 2008). In addition, when embedded in mixed phase or ice clouds, BC-containing particles modify the cloud properties, making them relevant for the understanding of the aerosol indirect effect's calculation (DeMott et al., 1999). Unlike greenhouse gases, BC-containing particles have a short lifetime in the atmosphere and are estimated to be removed via wet deposition within 5–11 days (Koch et al., 2009), making the reduction in BC-containing particle emissions an attractive option to mitigate global warming (Shindell et al., 2012). However, a more accurate lifetime description is needed to assess the influence of the BC-containing particles on the earth's radiative balance using three-dimensional models (Solomon et al., 2007).

The activation of BC-containing particles to cloud droplets is the main removal mechanism of BC (Vignati et al., 2010). However the ability of BC-containing particles to act as cloud condensation nuclei (CCN) depends on their size and on the relative amount of water-soluble coatings (Dusek et al., 2006; Rose et al., 2011). The composition of combustion particles is tightly linked to their origin, i.e. they can be emitted as pure BC or along with primary organic matter (POM) or inorganic compounds (Chirico et al., 2010; Heringa et al., 2011). Further non-refractory matter is acquired by the BC particles through ageing processes in the atmosphere, including condensation of compounds with sufficiently low volatility (organic or inorganic), coagulation and cloud processing (Cozic et al., 2007; Kuwata and Kondo, 2008; Schwarz et al., 2008b).

As a result of this ageing, the BC particles acquire coatings which make them more hygroscopic and more CCN active (Kuwata and Kondo, 2008; Tritscher et al., 2011). In addition, the mass absorption coefficient (MAC) of BC is size dependent and is amplified by coatings of non-refractory matter, resulting in a stronger direct effect on the earth's radiative balance (Schnaiter et al., 2005). The measurement of BC core size and mixing state is therefore of importance in order to better understand the BC removal mechanism and to model the climate impacts of BC.

The mixing state of atmospheric BC is however difficult to measure and previous studies are rare. For example, the aerosol's mixing state can be determined using a hygroscopicity tandem differential mobility analyzer (HTDMA), as summarised by Swietlicki et al. (2008) in their review study. A monodisperse measurement of the CCN concentration using a continuous-flow cloud condensation nuclei counter (CCNC) can also be used to obtain information on the mixing state of the aerosol (e.g. Rose et al., 2011; Jurányi et al., 2012). However, these two methods can only distinguish between particles of different hygroscopicity, whereas different compounds or different mixtures with equal hygroscopicity remain unresolved. Consequently, no information on the BC mixing state can be obtained using these techniques.

The aerosol time-of-flight mass spectrometer (ATOFMS; Sullivan and Prather, 2005) and similar instruments can provide information on the size-resolved chemical composition and degree of internal mixing state of absorbing particles with diameters under vacuum (D_{va}; DeCarlo et al., 2004) between 100–3000 nm. Healy et al. (2012) used the

ATOFMS to retrieve the mixing state of elemental carbon (EC) in Paris. The term EC is here employed instead of BC as the ATOFMS uses mass spectrometry rather than light absorption as the method of detection. In Paris, the smaller EC-containing particles ($D_{va} \leqslant 400$ nm) were mainly externally mixed, indicating local or regional sources, while bigger EC-containing particles $D_{va} \geqslant 400$ nm) were mainly internally mixed with nitrate compounds, indicating medium- to long-range transport.

More detailed information on the mixing state of BC can be obtained by combining multiple instruments. Herich et al. (2008) coupled an ATOFMS in series to a HTDMA in order to determine the mixing state of EC at the urban site Zurich (Switzerland) and at the high alpine site Jungfraujoch (Switzerland). In Zurich, EC-containing particles were found to be mainly internally mixed but still with the lowest affinity to water while no significant enhancement of EC at low GF could be found at the Jungfraujoch. By coupling a HTDMA-CCNC and a volatility tandem differential mobility analyser, Kuwata and Kondo (2008) characterized the CCN activity and volatility of hygroscopicity-selected particles and found a clear enhancement in the number fraction of BC particles in the particles with low volatility and a clear sensitivity of BC's CCN activity to the amount of coating.

The single particle soot photometer (SP2; Stephens et al., 2003) allows the determination of the mixing state of BC-containing particles within the atmospherically relevant BC size range (Schwarz et al., 2008a; Shiraiwa et al., 2008). McMeeking et al. (2011a) coupled it in series to a HTDMA and found that the dominant fraction of BC-containing particles, at an urban site in Manchester (UK) were non- or slightly hygroscopic particles. As a result, BC is expected to be much less CCN active than BC free particles of equal size (at equal supersaturation).

With 47 % of the world population living in cities and high BC concentrations, BC emitted in cities represents an important part of the total BC emissions and an important health hazard. Several studies performed in cities have shown that BC is emitted uncoated and that they gain coating after several hours although internally mixed BC can also be found in cities when transported from other places (Shiraiwa et al., 2008; Cheng et al., 2009; McMeeking et al., 2011b).

Paris, 2nd largest Megacity in Europe (after London), holds a quarter of France's population, but only a few studies have characterized the BC properties there (Liousse and Cachier, 1992; Ruellan and Cachier, 2001; Sciare et al., 2010; Healy et al., 2012). Liousse and Cachier (1992) highlighted the influence of meteorological conditions on BC concentrations while Ruellan and Cachier (2001) observed a strong influence of traffic on the BC concentration in downtown Paris. In addition, Sciare et al. (2010) found a strong local pattern of the carbonaceous aerosol.

In this study, a measurement campaign was carried out in Paris as part of the MEGAPOLI European project (megacity: emission, urban, regional and global atmospheric pollution and climate effects, and integrated tools for assessment and mitigation; www.megapoli.info) where the physical properties, mixing state and hygroscopicity of BC-containing particles were characterised.

2 Methods

2.1 Single particle soot photometer (SP2)

2.1.1 Description

The SP2, manufactured by Droplet Measurement Technology, Boulder, has previously been described in detail elsewhere (Stephens et al., 2003; Schwarz et al., 2006). In short, the SP2 uses laser-induced incandescence to quantify the BC mass in single particles. A continuous intra-cavity laser beam (Nd:YAG; $\lambda = 1064$ nm) is used to heat BC-containing particles to their vaporisation point. The peak intensity of the thermal radiation (measured at two different wavelength ranges), emitted by the incandescent BC core and detected by the SP2, is linearly proportional to the mass of refractory black carbon (rBC[1]) in the particle. This method is unbiased by the presence of non-refractory matter, which vaporises before the BC vaporisation temperature of T = 4000 K and the peak intensity of the incandescent light are reached (Moteki and Kondo, 2007). This method allows the quantification, with 100 % efficiency, of BC mass in individual particles between ∼ 0.5–50 fg BC per particle, corresponding to BC cores with mass equivalent diameters (D_{MEV}) between ∼ 80–500 nm (assuming a void free material density of 1800 kg m^{-3} for the BC core).

2.1.2 Calibration

Prior to the measurement field campaign, the SP2 was adjusted following the recommended adjustments detailed in Laborde et al. (2012b). The incandescence signal was calibrated (three times, at the beginning, half way through and at the end of the measurement campaign) using mobility size selected fullerene soot particles (Alpha Aesar; #FS12S011) which is recommended for SP2 calibration as it gives similar SP2 responses as ambient BC (Moteki and Kondo, 2010; Baumgardner et al., 2012; Laborde et al., 2012a). The fullerene soot particles were selected by mobility diameter using a differential mobility analyser (DMA) and the corresponding particles masses were calculated using the effective density data provided in Gysel et al. (2011). The scattering signal was calibrated twice (at the beginning and half way through the measurement campaign) using spherical polystyrene latex size standards with a diameter of 269 nm (Thermo Scientific, formerly Duke Scientific). More details on SP2 calibration

---

[1] The terms elemental carbon (EC), equivalent black carbon (EBC) and refractory black carbon (rBC) are operationally defined based on the applied measurement technique (thermal-optical, light absorption and laser-induced incandescence, respectively). However, they synonymously refer to pure carbon, e.g. Kondo et al. (2011), which is the most refractory and light absorbing component of carbonaceous combustion particles. Hereafter we use the term “BC” instead of “rBC” for the pure carbon measured by the SP2.

and calibration standard material can be found in Baumgardner et al. (2012), Laborde et al. (2012b) and Gysel et al. (2011).

2.1.3 Data analysis and uncertainties

The BC mass in individual particles is determined from the peak intensity of the incandescence signal and applying the fullerene soot calibration described in Sect. 2.1.2. Mass equivalent BC core diameters, D_{MEV}, are calculated from the measured BC mass assuming a void-free density of 1800 $\mathrm{kg\,m^{-3}}$. The BC core mass size distributions, derived from 30-min intervals of single particle data, were fitted with a lognormal function in order to estimate the BC mass below the SP2's detection limit. All BC mass concentrations presented here are corrected for this missing mass, which accounted for less than 10 % of the total mass on average.

In addition to the BC mass, the measurement of the light scattered by the particle allows the determination of its scattering cross section. However, the scattering cross section of BC-containing particles is decreasing soon after they enter the laser beam due to coating evaporation. The initial particle cross section can only be determined from the leading edge of the scattering signal (LEO-fit, Gao et al., 2007). Here the leading edge could only be considered up to 1 % of maximal laser intensity without interference from coating evaporation. The particle's optical diameter is then inferred from the measured scattering cross section using a Mie model that idealises the morphology of the BC-containing particles as a spherical BC core with a concentric shell of coating matter (Schwarz et al., 2008b). Refractive indices for both the non-refractory matter (n_{coat}) and the BC core (n_{BCcore}) have to be assumed in order to do so. The coating thickness, Δ_{coat}, of the BC core by non-refractory matter is then calculated as the difference between the whole particle optical radius and the BC core mass equivalent radius.

Inadequacy of the assumption made for the Mie calculations regarding particle morphology (sphericity) as well as refractive indices of the BC core (n_{BCcore}) and the coating (n_{coat}) can result in systematically biased optical sizes and derived coating thickness values. The LEO-fit method introduces additional random noise.

Purely scattering particles can be assumed to be spherical, leaving the choice of n_{coat} as the main source of bias. Here we measured size-selected ambient samples behind a DMA in order identify the optimum n_{coat} value. Agreement between optical diameter and mobility diameter was achieved for $n_{\mathrm{coat}} = 1.5$, which is in the range of refractive indices of inorganic salts ($(NH_4)_2SO_4 = 1.51$; NaCl = 1.53; Toon et al., 1976) and secondary organic aerosol index of refraction (~ 1.44–1.5; Schnaiter et al., 2003; Nakayama et al., 2010), at $\lambda = 1064$ nm.

Uncoated BC particles are known to be highly non-spherical aggregates of primary particles. However, Moteki et al. (2010) showed that the optical shape factor is not far away from unity for small size parameters (note, the SP2 uses a long wavelength). Furthermore, a good agreement (±10 %) between the optical diameter of the bare BC core, as determined after coating evaporation and before incandescence, and the BC core mass equivalent diameter was obtained using literature value of $n_{\mathrm{BCcore}} = 2.26 + 1.26i$ at $\lambda = 1064$ nm (Moteki et al., 2010). This result indicates reliable optical sizing of the bare BC cores with the above assumptions. The resulting systematic uncertainty of coating thickness values of uncoated BC particles with a mass equivalent diameter of 200 nm is estimated to be ±10 nm at $\Delta_{\mathrm{coat}} = 0$ nm. Systematically negative coating thickness values within this tolerance are thus not a concern, while single particle data can have even more negative values due to random noise (as seen in Fig. 10).

Thickly coated BC particles are also expected to be almost spherical. The optical sizing of thickly coated BC particles, derived with above assumptions for n_{coat} and n_{BCcore}, was also successfully verified against the mobility diameter of size-selected ambient samples. The mass equivalent diameter of the BC core is also determined with high accuracy (~ 10 % uncertainty of BC mass measurement; Laborde et al., 2012b). These results highlight the fact that accurate coating thickness is also obtained for thickly coated BC particles.

BC-containing particles with medium to thin coating are less spherical than highly coated particles but more spherical than uncoated particles. The accuracy of coating thickness values determined in these cases was not independently verified. However, it can be expected to be reasonably accurate too, as the assumption made in the Mie calculations performed well for uncoated and thickly coated BC particles.

2.2 Hygroscopicity tandem differential mobility analyser (HTDMA)

The HTDMA used in this study has previously been described in detail (Tritscher et al., 2011). Briefly, the aerosol is dried to a low relative humidity (RH ≤ 10 %) and brought to charge equilibrium with a ^{85}Kr bipolar charger before a first DMA (custom-built long DMA similar to TSI 3081) is used to select a quasi-monodisperse sample with a well defined dry mobility diameter (D_0) which is then humidified, to high RH (plug flow residence time of 26 s). A second DMA scans the humidified particles by mobility diameter (D_{RH}), which are then counted with a condensation particle counter (CPC, TSI 3022A). The hygroscopic growth factor of a particle is defined as $\mathrm{GF(RH)} = D_{\mathrm{RH}}/D_0$. The DMAs and humidifier are situated in a temperature controlled housing at 20 °C to guarantee accurate RH control and GF measurement.

Details on the data inversion procedures for HTDMA data are provided in Gysel et al. (2009). Briefly, sizing differences between the first and second DMA are corrected for with dry measurements of ambient air. Accurate operation of the HTDMA was verified with pure ammonium sulphate aerosol particles. The RH and growth factor accuracy are typically better than ± 1.2 % and ± 2 %, respectively. The growth factor probability density function (GF-PDF) was retrieved from the raw data using the TDMAinv inversion algorithm (Gysel et al., 2009).

The HTDMA was operated at a nominal RH of 90 %. Only measurements taken between 88 and 92 % RH were considered in the results and all inverted GF-PDFs were recalculated from the measured RH to the nominal RH of 90 %, following the approach descrived in Gysel et al. (2009). Particles with dry mobility diameters of $D_0 = 35$, 50, 75, 110, 165 and 265 nm were sequentially monitored but only results for $D_0 = 110$, 265 nm are presented here due to the overlap with the SP2 detection range.

2.3 Additional dataset used

The chemical composition of the non-refractory (at $T = 600\,^{\circ}\mathrm{C}$) components of particles (such as organics, sulfate, nitrate, ammonium and chloride) with diameters $D_p \leqslant 1\,\mu\mathrm{m}$ (NR-PM$_1$) was determined using a high resolution time-of-flight aerosol mass spectrometer (HR-ToF-AMS; collection efficiency 0.5; DeCarlo et al., 2006; Aerodyne Research Inc.). Positive matrix factorization (PMF; Ulbrich et al., 2009) was applied to the data set and the following four factors were found to explain most of the organic concentration's variability: biomass burning organic aerosol (BBOA), oxidized organic aerosol (OOA), hydrocarbon-like organic aerosol (HOA) and organic aerosol from cooking origin (COA). In this study, the PMF factors are only used to identify periods with a dominant influence from different aerosol sources, while complete results from the HR-ToF-AMS dataset will be found elsewhere (Crippa et al., 2012). However, it is important to notice that a high correlation between the BBOA factor time series and the levoglucosan time series (a typical biomass burning tracer) was observed, reinforcing the source apportionment results.

The light absorption coefficient of the aerosol was measured using an aethalometer (Magee scientific, AE-7) equipped with 7 light emitting diodes (LEDs) as light sources ($\lambda = 370$, 470, 520, 590, 630, 660, 880, 950 nm). The measurement was corrected for the shadowing effect and filter loading using the method from Weingartner et al. (2003) (a $C = 4.2$ was obtained from comparison with a multi angle absorption photometer, MAAP, during short periods, and $f = 1.3$ was used). A single correction factor C was used here for the entire measurement campaign due to a lack of MAAP data. Implications of this assumption will be discussed further down.

The aerosol size-distribution was measured using PSI's custom-built scanning mobility particle sizer (SMPS), with an aerosol to sheath flow ratio of 1 : 10. The performance of this SMPS was successfully verified during an SMPS intercomparison campaign (Wiedensohler et al., 2012).

A high sensitivity proton transfer reaction mass spectrometer (HS-PTRMS, Ionicon Analytik, Lindinger et al., 1998) was deployed during the intensive field campaign in order to quantify volatile organic compounds (VOCs). A 10 m Teflon tubing sampling line was installed on the roof of the building with a primary flow of 10 $\mathrm{l\,min^{-1}}$. During the campaign, 39 mass to charge ratios (m/z) were monitored with a temporal resolution of 2.5 min, including the ions at $m/z = 25$, 32, 37, 39, 55, 80 used to control the HS-PTRMS performance (fragmentation, ionisation) while the 33 remaining m/z ions monitored correspond to individual VOC's or sum of isomers. The transmission of the PTR-MS quadrupole was adjusted using the mean of 18 individual VOCs with certified concentration overlapping the mass range of the VOCs monitored within the field campaign. Within this study two VOC's measured by PTRMS were considered: benzene (m/z 79) and toluene (m/z 93). The two selected VOCs were also individually calibrated in the range 0.2–8 ppb at 50 % RH and are here used as an indicator of air mass age.

To identify the origin of sampled air masses, retroplumes were calculated using the Lagrangian particle dispersion model FLEXPART (Stohl et al., 1998, 2005). FLEXPART was driven with data from the European centre for medium-range weather forecasts (ECMWF) with 0.18 °C resolution over Europe (1 °C over the rest of the globe). Retroplumes were calculated every three hours for the SIRTA site by releasing 60 000 particles in a small box, centered at the measurement location and tracking them back in time for 20 days. The primary model output is an emission sensitivity, which is proportional to the particle residence time. Emission sensitivity was calculated for a passive tracer, not taking into account wet and dry deposition. The emission sensitivity value ($\mathrm{s\,kg^{-1}}$) is a measure for the simulated mixing ratio at the measurement site that a source of unit strength ($\mathrm{kg\,s^{-1}}$) would produce. The footprint sensitivities used here represent the pollution in the lowest model layer (0–100 m a.g.l.).

2.4 Köhler theory

The following method was used in order to calculate the theoretical curves shown in Fig. 14e–h. The equilibrium between a solution droplet and water vapour is described by Köhler theory (e.g. McFiggans et al., 2006). Petters and Kreidenweis (2007) introduced an empirical parametrisation to describe the relationship between GF and water activity (a_w) using a single hygroscopicity parameter (κ).

$$\mathrm{GF}(a_\mathrm{w}) = \left(1 + \kappa \frac{a_\mathrm{w}}{1 - a_\mathrm{w}}\right)^{1/3} \tag{1}$$

The Köhler equation describes the relationship between water activity and equilibrium RH over a droplet:

$$\exp\left(\frac{4\sigma_\mathrm{sol} M_\mathrm{w}}{RT\rho_\mathrm{w}\,\mathrm{GF}\,D_0}\right) = \frac{\mathrm{RH}}{a_\mathrm{w}}, \tag{2}$$

where M_w, ρ_w are the molecular weight and the density of water, respectively, R is the ideal gas constant, T is the temperature in Kelvin, σ_sol is the surface tension of the solution droplet and D_0 is the dry diameter of the particle. The equilibrium GF for a certain κ and RH is obtained, for a certain κ and D_0, by numerically solving Eqs. (1) and (2). σ_sol is thereby assumed to be equal to the surface tension of pure water for all calculations.

The relative humidity is commonly expressed as supersaturation ($\mathrm{SS} = \mathrm{RH} - 1$) in the context of cloud condensation nuclei (CCN) activation. The critical supersaturation for CCN activation corresponds to the maximum equilibrium SS as a function of the GF, which is also obtained by numerically solving Eqs. (1) and (2), for a certain κ and D_0.

The Zdanovski-Stokes-Robinson (ZSR) mixing rule, which has been shown to perform well for ambient aerosols (e.g. Gysel et al., 2007), can be used to calculate the hygroscopic parameter κ of a mixed particle from pure component properties. The kappa value of a mixed particle (κ_{mixed}) becomes (Petters and Kreidenweis, 2007):

$$\kappa_{\text{mixed}} = \sum_i \varepsilon_i \, \kappa_i \tag{3}$$

where κ_i is the hygroscopicity parameter of component i and ε_i its volume fraction in the dry mixed particle. The κ value of the insoluble BC core is 0. Equation (3) simplifies then to:

$$\kappa_{\text{mixed}} = \varepsilon_{\text{coat}} \, \kappa_{\text{coat}} = \left(1 - \frac{(D_{\text{MEV}})^3}{(D_{\text{MEV}} + 2\,\Delta_{\text{coat}})^3}\right) \kappa_{\text{coat}} \tag{4}$$

for coated BC particles, where the suffix “coat” denotes the non-refractory coating. The growth factor and the critical supersaturation as a function of the coating thickness, shown in Fig. 14e–h are then obtained by inserting κ_{mixed} from Eq. (4) in Eqs. (1) and (2), followed by numerical solving, as described above.

2.5 Measurement site and experimental setup

As part of the MEGAPOLI project, three stationary measurement stations were chosen in greater Paris: one down-town (laboratoire d’hygiène de la ville de Paris, LHVP), one north-east of the city (golf de la poudrière) and one south-west of it (site instrumental de recherche par télédetection atmosphérique, SIRTA). Additionally, mobile measurements were performed on-board of two aircrafts and two vans. This study focuses on the measurements performed from 15 January 2010 to 15 February 2010, on the SIRTA measurement platform (Haeffelin et al., 2005), situated ~30 km south-west of Paris city centre (Fig. 1), on the Ecole Polytechnique campus.

The above mentioned instruments (apart from the PTRMS) were installed in an air-conditioned trailer, on the SIRTA measurement platform. A common inlet, equipped with a PM_{10} head was set up through the trailer’s side wall and reached 5 m above ground (Fig. 2). All instruments were sampling in parallel from the common inlet and the total flow was adjusted, using an extra pump, to the required 16.7 l min^{-1} in order to obtain the size cut at a diameter of 10 µm. The SP2 and HTDMA setup was changed during two days (30 January–1 February 2010) when they were sampling in series (coupled setup, Fig. 2b) in order to investigate the particle mixing state as a function of the diameter and hygroscopic growth factor. The HS-PTRMS was installed in downtown Paris on the LVHP measurement platform.

3 Results and discussion

3.1 Time series

The time series of the data from the SP2, the HS-PTRMS, the SMPS, the HR-ToF-AMS and the aethalometer are presented in Fig. 3.

The observed BC mass concentration is ~ 0.9 µg m^{-3} ± 0.7 µg m^{-3} (average ± standard deviation) although increasing to 4 µg m^{-3} for several days: 26–27 January and 7–9 February (Fig. 3a). The episodes, characterized by the highest BC mass concentrations, will be named “Continental” period, as they were influenced by aged air masses from Continental Europe according to the retroplume analysis (Fig. 4a). The BC mass concentrations observed in Paris are similar to previously reported values in various European highly populated cities, although different methods were used, i.e. ~ 3 µg m^{-3} in Milano (Invernizzi et al., 2011), ~ 1.7 µg m^{-3} in Barcelona and ~ 2 µg m^{-3} London, urban background (Reche et al., 2011) and ~ 0.7 µg m^{-3} in Mexico City (Subramanian et al., 2010).

The BC core mass size distribution, shown in Fig. 5 as a function of the BC core mass equivalent diameters (D_{MEV}), is also rather stable throughout the month with a modal diameter peaking around 150 nm and most BC mass is found between $D_{\mathrm{MEV}} \approx$ 100–200 nm. An exception is the “Continental” period, with unusually large BC core diameters: the modal diameter occasionally increases up to the SP2 detection limit of ~ 600 nm and is on average around 230 nm. Possible reasons for the larger core sizes during the “Continental” period as well as the influence of different air mass types will be discussed in Sect. 3.3.2. A slight increase in the BC core size ($D_{\mathrm{MEV}} \sim 220$ nm) was also reported by Shiraiwa et al. (2008) when aged air masses were measured. Apart from this episode, the range of the BC core D_{MEV} observed here is consistent with the range reported by a previous study where BC core D_{MEV} values from an urban air mass and an air mass influenced by biomass burning were reported to be around 150 nm and 200 nm, respectively (Schwarz et al., 2008a).

The median thickness of non-refractory coatings on the BC cores is shown in Fig. 3b for particles with BC core diameters between $D_{\mathrm{MEV}} = 180$–220 nm. The median coating thickness is on average $\Delta_{\mathrm{coat}} = 33\,\mathrm{nm} \pm 35\,\mathrm{nm}$ (average ± standard deviation), though peaking to over 100 nm during the “Continental” period.

The particle number concentration detected by the SP2 is shown in Fig. 3c, split by totally detected particles, BC-containing particles and purely scattering particles (“purely scattering” meaning no BC core or a BC core below the SP2’s lower detection limit of ~0.5 fg BC corresponding to a D_{MEV} of 80 nm). Most of the time the majority of the particles are purely scattering, though occasionally almost all detected particles contain a BC core (e.g. 18 and 25 January 2010). The total number concentration of particles with a mobility diameter ≥ 20 nm measured by the SMPS (thick green line in Fig. 3d) is substantially higher compared to the SP2 measurement, as many particles fall below the SP2’s detection limit. Restricting the SMPS number concentration to particles with mobility diameters ≥ 140 nm, corresponding to the lower detection limit of the SP2 for purely scattering particles, reveals excellent agreement with the SP2, thereby indicating good performance of both instruments. The BC-containing particles detected by the SP2 account for 0–15 % of all particles detected by the SMPS (Fig. 3d). These numbers have to be interpreted with care as often more than 50 % (by number) of the BC cores fall below the SP2’s lower detection limit. Nevertheless, the contribution of BC-containing particles to the total particle number concentration varies considerably and it is obvious that not all particles contain a BC core, even with generous allowance for the undetected BC cores. The BC mass fraction in PM_1 (PM_1 calculated as the sum of NR-PM_1 measured by the HR-ToF-AMS and the BC mass measured by the SP2) is higher than the BC number fraction, accounting for ~ 15 % on average and increasing up to 40 % during a few days (e.g. 28 January, 5–6 February; Fig. 3e). Several studies have reported similar contribution of BC to PM_{10} (total mass of all particles with an aerodynamic diameter $\leqslant 10\,\mu m$) in various European highly populated cities, although different methods were used: Milano (10–22 %; Invernizzi et al., 2011) and in London (10–26 %; Reche et al., 2011). However, lower BC mass fractions in PM_{10} were observed in urban background sites in Barcelona (5 %; Reche et al., 2011) and in Mexico (~ 1.5 %; Subramanian et al., 2010; Querol et al., 2008) which may be due to an additional dust source. Substantial differences between the relative contributions of BC to PM_1 and PM_{10} can be expected where significant dust influence occurs. Indeed BC mainly contributes to PM_1 whereas dust mainly contributes to PM_{10}.

The temporal variability of the aerosol hygroscopic properties is shown in Fig. 6 for the example of particles with a dry mobility diameter of $D_0 = 265\,\text{nm}$. The mean GF of all particles (Fig. 6, black line) varies between 1.2 and 1.7 at 90 % RH. The growth factor probability distribution function (GF-PDFs), shown as contour plot in (Fig. 6a), reveals that the variability of the mean GF is mostly driven by varying relative contributions of background aerosol with a modal GF of ~ 1.6 and recently emitted non- and slightly hygroscopic aerosol with a modal GF between 1.0 and 1.2. Moderately hygroscopic particles with GFs in the range of 1.2–1.4, likely moderately aged emissions of regional origin, are occasionally present. The averaged GF-PDF, shown in Fig. 6b, reveals that the most hygroscopic background particles dominate at $D_0 = 265\,\text{nm}$, followed by the recently emitted non- and slightly hygroscopic particles and the moderately (or medium) hygroscopic particles.

The observed variations of BC concentrations, BC properties and aerosol hygroscopicity can have many reasons such as e.g. varying contributions of different sources, dilution with background air and atmospheric ageing processes. Several studies have examined how the ratio between the toluene and benzene mixing ratios (T/B) can provide insight into sources of pollution as well as the photochemical age of the air mass.

Typically, high T/B values are associated with fresh traffic emissions while lower values are associated with more photochemical degradation. The threshold between high and low T/B values is reported to be around 2.45 with regional differences attributable to different vehicle types and fuel composition (Khoder, 2007; Hoque et al., 2008). The measurement of toluene and benzene concentrations were only performed at the LHVP site downtown Paris, 30 km away from the measurement site of this study. The T/B values at SIRTA are therefore not expected to be perfectly equal to those measured at the LHVP site due to different local influences. Nevertheless, many aerosol properties were shown to be highly correlated across the three measurement sites of the MEGAPOLI project (Beekmann et al., 2012), highlighting the similarities of the air masses measured at the sites. The T/B values from downtown Paris can therefore be expected to provide meaningful information for the SIRTA site too, although differences may be present for the freshly emitted aerosol and PMF results will also be used to identified sources. Throughout the measurement campaign, the T/B values (Fig. 3f) were low during several long periods (e.g. T/B ~ 0.8; 26–28 January; 7–13 February) and high during many short periods (e.g. T/B ~ 5–7; 18 January 10:30 a.m. local time: LT; 22 January 10:50 a.m. LT; 4 February 09:50 a.m. LT). The observation of both high and low T/B values indicates different episodes with varying relative influence from fresh traffic emissions and aged air masses, respectively.

Biomass burning influence can be identified from the wavelength (λ) dependence of the absorption coefficient (α) of the aerosol. $\alpha(\lambda)$ is typically a power function of λ (see e.g. Moosmüller et al., 2011, for more details):

$$\alpha(\lambda) = \text{const}\,\lambda^{-\text{AAC}} \tag{5}$$

with the absorption Ångström coefficient (AAC) as exponent. From Eq. (5), follows (Moosmüller et al., 2011):

$$\text{AAC}(\lambda) = -\frac{d\ln(\alpha)}{d\ln(\lambda)} \tag{6}$$

In this study, the AAC was determined by linearly fitting the absorption spectrum $\alpha(\lambda)$ in log-log space, using 5-min averages of the aethalometer data at all 7 wavelengths.

The observed AAC are shown in Fig. 3g. Values around 2 are typically associated with biomass burning emissions while values around 1 are associated with traffic emissions (Sandradewi et al., 2008). Strong biomass burning influence episodes (e.g. 31 January 12:00 a.m.–09:00 p.m. LT; 1 February 12:00 a.m. LT) and sharp traffic influence episodes (e.g. 31 January 02:00 p.m. LT; 3 February 12:00 p.m. LT) can be identified during the measurement campaign.

The above results revealed considerable variability of BC concentrations and properties. The T/B and AAC values provide evidence of episodes with dominant influence from traffic emissions, biomass burning or aged background aerosols. This is further confirmed by statistical analysis of the organic mass spectra measured by the HR-ToF-AMS. The PMF analysis (see Sect. 2.3) identified four components of the organic aerosol: HOA, BBOA, OOA and COA each of them with considerable contributions at times (Crippa et al., 2012). In order to assess the relative contributions of traffic and biomass burning to the BC mass concentrations encountered at the SIRTA site, a simple bilinear regression model was used, which is based on the co-emission of BC and organic species by the different sources. The basic assumption is that, at any time (t), all BC mass ($m_{\text{BC,tot}}$) is coming from biomass burning ($m_{\text{BC,BB}}$) or traffic ($m_{\text{BC,traff}}$) emissions:

$$m_{\text{BC,tot}}(t) = m_{\text{BC,BB}}(t) + m_{\text{BC,traff}}(t) \tag{7}$$

The BC mass emission from biomass burning is assumed to be proportional to the mass of BBOA (m_{BBOA}) released, with a constant proportionality factor a:

$$m_{\text{BC,BB}}(t) = a\, m_{\text{BBOA}}(t) \tag{8}$$

The BC mass emission from traffic is assumed to be proportional to the mass of HOA (m_{HOA}) released, with a constant proportionality factor b:

$$m_{\text{BC,traff}}(t) = b\, m_{\text{HOA}}(t) \tag{9}$$

Combining Eqs. (7)–(9) provides the bilinear regression model with the free regression parameters a and b, which is fitted to the time-resolved BC mass concentration measured by the SP2 ($m_{\mathrm{BC,tot}}$) and PMF results for the AMS data (m_{HOA}, m_{BBOA}):

$$m_{\mathrm{BC,tot}}(t) = a\, m_{\mathrm{BBOA}}(t) + b\, m_{\mathrm{HOA}}(t) \tag{10}$$

This simple approach is expected to work best when fresh emissions give the dominant contribution to BC mass, while atmospheric ageing and removal processes will vary the ratio between the PMF factors and the associated BC mass. For this reason, the bilinear regression was done in two steps. In a first step the regression was applied to the whole data set in order to identify the periods when the regression performs well. In a second step, the regression was repeated with restricting the data set to those times, when the first regression step predicted the measurement within ± 20 %. This particular data selection was chosen, as good regression performance is thought to be an indicator of dominant influence from primary emissions. The second regression step eventually had only a small influence on the retrieved proportionality factors a and b, compared to those obtained after the first step. The result of the second step is reported in the following as it is thought to be more accurate.

The results of the bilinear regression are shown in Fig. 7a and b, in absolute and relative terms, respectively. The whole SP2 data set is shown in dark blue in Fig. 7a and b, while the data points used for the restricted regression are shown in light blue in Fig. 7b. The modelled BC mass concentration is calculated for the whole data set (Fig. 7a, green line) using the coefficients fitted to the restricted data set. The simple bilinear regression performs surprisingly well for the whole data set, with 32 % and 80 % of all data points falling within the limits of ± 20 % and a factor of 2, respectively. The model frequently underpredicts BC mass concentration between 26–29 January and 4–8 February, when aged continental air mass is encountered. Overprediction is frequently obtained between 16–23 January, when an influence from both aged background air and biomass burning was observed. The regression coefficients a and b were found to be 0.002 (±0.008) and 0.84 (±0.01), respectively. The respective fractional contributions Q_{traff} and Q_{BB} of the traffic and biomass burning emissions to the observed BC mass are then obtained from the regression results with the following equations, where the bars indicate averaging over the whole data set:

$$Q_{\mathrm{Traff}} = \frac{\overline{m_{\mathrm{BC_{traff}}}}}{\overline{m_{\mathrm{BC_{Tot}}}}} \tag{11}$$

$$Q_{\mathrm{BB}} = \frac{\overline{m_{\mathrm{BC_{BB}}}}}{\overline{m_{\mathrm{BC_{Tot}}}}} \tag{12}$$

The traffic and biomass burning emissions were found to account for $Q_{\mathrm{traff}} = 99.6\,\%$ and $Q_{\mathrm{BB}} = 0.4\,\%$ of the total BC mass according to the simple bilinear regression model. This result is most likely biased to traffic emissions, as biomass burning is expected to give some minor contribution to BC mass, too. The relative contribution of the fragment *m/z* 60, a marker for biomass burning aerosol, was actually somewhat higher in the HOA factor retrieved from this data set compared to other data sets. This gives evidence that the HOA factor contains a minor biomass burning contribution, which would explain a small bias of the regression model to traffic emissions. Nevertheless, the above result indicates that traffic is the dominant source of BC in Paris, which is qualitatively consistent with 74 % traffic contribution, determined by Crippa et al. (2012) for the same location and time period using the observed AAC value for the source apportionment following the approach by Sandradewi et al. (2008), and with 88 % traffic contribution, determined by Healy et al. (2012) for the city centre of Paris during the same time period using data from an aerosol time-of-flight mass spectrometer (ATOFMS). This result contrasts with previous result from Holme Moss, UK (Liu et al., 2011) where solid fuel burning and traffic emission influenced equally BC mass concentrations (the coefficients found were $a = 0.51$ and $b = 0.62$ in this case).

3.2 Diurnal cycles

Further insights into the influence of traffic and biomass burning emissions on aerosol concentrations and properties can be obtained by the analysis of diurnal patterns. The BC mass concentration (Fig. 8a), the number fraction of BC-containing particles (Fig. 8b, calculated as the number of BC particles detected by the SP2 divided by the total number of particles detected by the SMPS), the HOA mass concentration (Fig. 8c) and the number fraction of non-hygroscopic particles with a GF ≤ 1.05 at RH = 90 % and $D_0 = 265$ nm (Fig. 8d) all exhibit very similar diurnal patterns with minimal values during night-time and distinct peaks during the morning and evening rush hours. Similar diurnal variations were found for the non-hygroscopic particles, in Milano, by Baltensperger et al. (2002). The ACC – low and high values (Fig. 8f) indicate influence from traffic and biomass burning emissions, respectively – and the BBOA mass concentration (Fig. 8g) follows a completely different pattern with low values during daytime, high values during night-time and a maximum at ∼ 10–11 p.m. LT. This pattern can most likely be attributed to a peak of domestic heating activities in the late evening hours. Similar diurnal variation can be observed when looking at the number fraction of slightly hygroscopic particles ($1.1 \leqslant \text{GF} \leqslant 1.2$). This indicates a link between biomass burning and the emission of slightly hygroscopic aerosol which will be corroborated in Sect. 3.3.5. The comparison of the diurnal patterns of BC mass concentration with traffic and biomass burning markers provides clear evidence that traffic emissions give the dominant contribution to BC mass concentrations and is consistent with the result of the bilinear regression model (Sect. 3.1). However, the evening peak of HOA is somewhat delayed compared to the evening peak of BC and it is close to the BBOA peak. This could indicate that the HOA factor contains some minor contribution from biomass burning, which would explain the over- and underestimation of the traffic and biomass burning contributions, respectively, by the bilinear regression model (Sect. 3.1).

Only a weak diurnal cycle was observed for the median thickness of non-refractory coatings on the BC cores with core diameters between $D_{\text{MEV}} = 180$–220 nm (Fig. 8e).

Nevertheless, two minima of the median coating thickness can be identified at the morning and evening rush hours, consistent with emissions of uncoated BC particles by traffic (see also Sect. 3.3.3). The fact that the observed diurnal variability is so small can either be explained with slow time scales for coating acquisition, leaving most BC particles with a rather thin coating, or with a rather constant ratio of fresh and aged BC particles throughout the day. However, the latter hypothesis is not really consistent with the pronounced diurnal cycle of, e.g. the toluene to benzene mixing ratios (T/B).

3.3 Aerosol properties for different sources/air mass types

Different sources of BC and air mass types were identified with above analyses. This section aims at investigating the properties of BC particles as a function of source and air mass type. Episodes with dominant influence from traffic emissions, biomass burning emissions, aged air mass and the "continental" air mass are first identified in order to compare various aerosol and BC properties between these episodes. The resulting time periods are indicated in Fig. 3 as the coloured bars.

3.3.1 Segregation criteria

A strong influence of biomass burning was identified using the PMF results. The time periods when the BBOA mass concentration was accounting for more than 30 % of the total organic mass measured by the HR-ToF-AMS were selected as "biomass burning influenced" (brown bars in Fig. 3b, d, f). These periods coincide with high AAC values, which confirm strong biomass burning influence. An example of a typical retroplume for those periods can be found in Fig. 4b, where a major contribution of the local sources can clearly be seen.

The "traffic influenced" time periods were selected using both the T/B value and the PMF results. The periods when T/B $\geq$ 3.5 (criterion for fresh traffic emission) and when the BBOA mass accounted for less than 15 % of the total organic mass concentration (criterion for minor biomass burning influence) were selected as traffic influenced (black bars in Fig. 3b, d, f).

Healy et al. (2012) already identified different time periods during the same measurement campaign, based on the same retroplume calculations. Two periods were associated with continental, aged air masses: 26–28 January and 7–15 February. This is consistent with low T/B values (Fig. 3f) and high OOA mass fractions (not shown) observed here for this period, which we already named "continental" period in Sect. 3.1. Short events when BBOA and HOA accounted for more than 35 % of the total organic mass, indicating substantial influence from local sources, were filtered from the continental period identified by Healy et al. (2012) in order to get undisturbed "continental" period for the following analyses (violet bars in Fig. 3b, d, f). An example of a typical retroplume experienced during those periods can be found in Fig. 4a, where a major contribution of the pollution from Eastern Europe is likely. A similar conclusion can be drawn for the second time period (7–9 February) from Fig. 4c although a slightly lower influence of the Eastern Europe pollution is observed, in favour of a high influence of the Benelux area.

Finally, the time periods when the OOA mass accounts for ≥ 65 % of the total organic mass, and not considering the "continental" periods, were selected to represent "aged air mass", as OOA mainly originates from secondary organic aerosol or aged primary organic aerosol. Westerly wind prevailed during this time period though with a strong potential influence of the local sources (Fig. 4d).

3.3.2 BC core mass size distribution

The BC core mass size distribution is reported in Fig. 9, where significant differences could be found for the four types of aerosol. The smallest BC cores are observed for the traffic influence (peak at $D_{\mathrm{MEV}} \approx 100$ nm; Fig. 9a), which is consistent with a previous study where traffic emitted BC core, D_{MEV}, were observed around 100 nm (Schwarz et al., 2008a). Biomass burning and aged aerosol influenced air masses are characterized by somewhat larger BC core sizes, peaking at $D_{\mathrm{MEV}} \approx 130$ and ≈ 160 nm, respectively (Fig. 9b, c), while the largest BC cores were observed for the continental air mass (peak at $D_{\mathrm{MEV}} \approx 200\,\mathrm{nm}$, occasionally much larger; Figs. 9d and 5a). Large BC-containing particles were also observed by Healy et al. (2012) for the continental air mass with a modal particle diameter of ~ 700–900 nm. However, the ATOFMS measures the vacuum aerodynamic diameter of the whole particle, as opposed to the BC core diameter measured by the SP2. Thus the size increase is most likely amplified in their case by the fact that the continental air mass was also characterised by the thickest non-refractory coatings (Sect. 3.1 and Sect. 3.3.3, Fig. 10a, b). Bigger BC cores in the aged continental air mass can either be the results of dominant influence from a different source or of atmospheric transformation (coagulation) and transport processes (wet removal). Shiraiwa et al. (2008) reported a slight increase of the modal BC core diameter in aged air masses, however, Moteki et al. (2012) reported a decrease of the modal BC core size during transport due to preferential wet removal of the bigger BC particles. A possible reason for the larger core sizes observed during the "continental" period would be the presence of a different source of BC such as coal burning.

3.3.3 BC core coating thickness

The coating thickness of the BC particles was determined from the SP2's light scattering and incandescence (BC mass) measurements assuming a spherical concentric core shell morphology for the Mie calculations (see Sect. 2.1.3 for details). The analysis of the coating thickness is here restricted to two different BC core size ranges ($D_{\mathrm{MEV}} = 180$–$220\,\mathrm{nm}$ and 240–280 nm) in order to investigate the size dependence of the coating thickness.

The normalised histogram of the coating thickness of non-refractory matter on BC cores with a D_{MEV} between 180–220 nm is reported, for the four aerosol types, in Fig. 10a. The histogram of the coating thickness for BC particles observed during traffic influence has a distinct peak at slightly negative coating thickness values (consistent with essentially uncoated BC particles within experimental uncertainty) although the histogram shows a "tail" which extends to higher coating thickness. Around 70 % of the particles have less than 10 nm coating thickness, clearly indicating that BC particles emitted by traffic are essentially uncoated. The high number fraction of uncoated particles results in a median coating thickness of 2 nm (see also Table 1). This is consistent with a BC mass fraction of ~ 85 %, as reported by (Chirico et al., 2010) which translates into a coating thickness of 5 nm at a core diameter of $D_{\text{MEV}} = 200$ nm. Previous studies, using the SP2, reported a slightly bigger median coating thickness of 20–30 nm for urban emission that aged for a few hours (~ 2h; Schwarz et al., 2008a; Shiraiwa et al., 2008). This small difference may to some extent be caused by the short ageing time, however, it is anyway close to the absolute uncertainty of coating thickness values determined with the SP2 (Sect. 2.1.3).

The coating thickness histogram for the aged aerosol air mass is also peaking at $\Delta_{\text{coat}} \approx 0$ nm but the number fraction of BC particles with medium and thick coatings ($\Delta_{\text{coat}} \geq 30$–200 nm) is higher compared to traffic influence. Indeed, the majority (~ 70 %) of the particles with BC $D_{\text{MEV}} \approx 200$ nm have a coating thickness of 10 nm or more (Fig. 10a, black dashed lines). As a result, the median coating thickness of non-refractory matter on the $D_{\text{MEV}} \sim 200$ nm BC cores is ~ 44 nm. This value is slightly lower than the average range 48–60 nm reported by Schwarz et al. (2008a) and Shiraiwa et al. (2008), for aged aerosol and the same BC core size range, indicating that the background aerosol observed in this study is either slightly less aged or contains a larger fraction of fresh emissions.

The coating thickness histogram of the continental air mass still peaks at $\Delta_{\text{coat}} \approx 0$ nm, similar to the aged air mass, however, the number fraction of coated particles ($\Delta_{\text{coat}} \geqslant 10$ nm) is even higher (~ 80 %), resulting in an average median coating thickness of as much as 93 nm. This is the highest value among the four identified air mass types and substantially larger than the ~ 48–60 nm reported by Shiraiwa et al. (2008) and Schwarz et al. (2008a) for aged aerosol, indicating a highly aged aerosol.

In the case of biomass burning influenced air mass, the coating thickness histogram is also peaking at slightly negative values (uncoated within experimental uncertainty) and half (~ 53 %) of the BC-containing particles have a coating thinner than 10 nm.

A substantial fraction of these uncoated particles are likely from the traffic emissions as biomass burning has been shown to give a minor contribution to BC mass (Sect. 3.1 and 3.2). Almost no particles with very thick ($\gtrsim 70$ nm) coating were observed, indicating the absence of an influence from aged aerosol. A slightly enhanced fraction of particles with a moderate coating (~ 20–40 nm) was observed compared to the traffic influence. These BC-containing particles with moderate coating are most likely from biomass burning emissions, as will be shown in more detail in Sect. 3.4. Schwarz et al. (2008a) reported an average coating of $\sim 65 \pm 12$ nm for BC from biomass burning, likely emitted by brush fires, which is much higher than the median coating thickness of ~ 15 nm observed here. This substantial difference is likely caused by the difference of the biomass burning sources, i.e. brush fire emissions may have a much higher OC to BC ratio than those from residential heating (Heringa et al., 2011; Hennigan et al., 2011).

The coating thickness of bigger BC cores with $D_{\mathrm{MEV}} = 240$–280 nm was analysed in the same way (Fig. 10b and Table 1). The observed coating thickness distribution is almost equal to that for the smaller BC cores. This applies also to the coating thickness distributions averaged over the whole campaign (Fig. 10c). On average, the fresh emissions and aged aerosol give similar contributions to the total number of BC particles with $D_{\mathrm{MEV}} = 180$ and 260 nm, which results in an overall mean coating thickness of ~ 32 nm, in between the extreme cases. Generally, the tail of coated BC particles is very broad, indicating a wide range of aging times in the aged background aerosol.

BC is insoluble in water. Thus a substantial fraction of the BC-containing particles can be expected to be non- or slightly hygroscopic, given the high number fraction of BC particles without or with very little coating. This further implies that they require much higher supersaturation for CCN activation compared to water-soluble particles of equal size. The composition of the coatings – highly hygroscopic inorganic salts as opposed to slightly hygroscopic organic matter – plays of course also a role. Detailed investigations on the relationship between coating thickness and hygroscopicity of BC-containing particles will be shown in Sect. 3.4.

3.3.4 Mass absorption coefficient

The mass absorption coefficient (MAC; also named mass absorption efficiency) of BC particles is defined as the light absorption cross section at a certain wavelength per unit mass of BC. The MAC is an important property of BC particles as it is, e.g. required to infer equivalent BC (EBC) mass from light absorption measurements and to calculate light absorption from modelled BC mass in radiative transfer simulations. The MAC is size dependent, peaking at a particle diameter equivalent to the incident wavelength and increases with coating thickness (Schnaiter et al., 2005). Great discrepancies exist between MACs reported in literature, partially due to measurement limitations (Bond and Bergstrom, 2006). The SP2 measures the mass of BC independently of the mixing state of the particles, thereby obtaining an accurate BC mass measurement. The MAC value is then calculated as the ratio of the light absorption coefficient (measured by the aethalometer, at $\lambda = 880\,\mathrm{nm}$) to the BC mass concentration.

The histogram (normalised to the area) of the measured MAC (10-min averages) is shown for the four air mass types (Fig. 11a) and the entire data set (Fig. 11c). The average for each air mass type is additionally reported in Fig. 11b. The MAC observed for the different air mass types are similar, but subtle differences exist (see also Table 1). The traffic influenced air mass exhibits the smallest average MAC ($\sim 7.3\,\mathrm{m^2\,g^{-1}}$), which is consistent with the fact that the BC cores are mainly uncoated and small (Figs. 9 and 10). Biomass burning influenced air mass is characterised by a somewhat larger average MAC ($\sim 7.8\,\mathrm{m^2\,g^{-1}}$) than traffic, which is consistent with somewhat thicker coating and a bigger core size. The aged aerosol shows the highest average MAC ($\sim 8.8\,\mathrm{m^2\,g^{-1}}$), which is consistent with thicker coating compared to traffic and biomass burning. On the other hand, the average MAC of the continental aerosol ($\sim 8.3\,\mathrm{m^2\,g^{-1}}$; Table 1) is similar to biomass burning MAC but smaller than aged aerosol. This is not quite consistent with the observation that the continental aerosol has the thickest coating. However, the continental aerosol has also been shown to have substantially larger BC core sizes than the other air mass type, which also has, together with morphology effects, an influence on the resulting MAC. Furthermore, the continental BC might have a different refractive index, if it was from a different source. The average MAC of the entire dataset is ~ 8.6 $m^2\,g^{-1}$ at 880 nm (Fig. 11c and Table 1). This MAC translates to ~ 13.6 $m^2\,g^{-1}$ at 550 nm (using Eq. 5 and assuming AAC = 1) (Fig. 11c and Table 1), which is higher than the value of 7.5 ± 1.2 $m^2\,g^{-1}$ reported by Bond and Bergstrom (2006) at the same wavelength. The difference may be explained by the fact that Bond and Bergstrom (2006) reported only freshly emitted BC MAC values or by an error in the absorption measurement. Indeed, as previously mentioned (Sect. 2.3), a single correction factor C was used here to correct the aethalometer data introducing a possible bias of up to 40 % if the BC type and size differs a lot for the time where C was calculated.

The width of the histogram is certainly partly due to experimental noise but part of the observed variability also reflects true differences between the air mass types (Fig. 11a).

3.3.5 Aerosol hygroscopicity

The particle hygroscopicity defines its affinity to take up water. In combination with the ambient supersaturation and the particle size, it determines whether or not a particle will activate as a cloud condensation nuclei, thereby increasing its chance of being removed from the atmosphere. Aerosols next to sources are often external mixtures of particles with different composition. Their hygroscopicity is therefore unique and important to be characterized (Rose et al., 2011). Here we investigate the hygroscopic mixing state of the aerosol for the four air mass types. A distinct mode of hygroscopic background aerosol with a GF of ~ 1.6 at 90 % RH is present during all air mass types for particles with a dry mobility diameter of D_0 = 265 nm (Fig. 12a–d). The background aerosol is dominant for the aged aerosol and the continental influenced air mass, accounting for ~ 84 % of all particles in either case (Fig. 12a, b). Its contribution decreases in the traffic and the biomass burning influenced air mass, accounting for 54 % and 34 %, respectively (Fig. 12c, d). For all periods, the relative contribution of the background aerosol decreases with decreasing particle dry size, as seen in Fig. 12 when

ACPD
12, 25121–25180, 2012

comparing panels a–d ($D_0 = 265$ nm) with panels e–h ($D_0 = 110$ nm). This statement also holds for the other dry mobility diameters, which are not shown here. This observation is consistent with previous literature (Swietlicki et al., 2008).

The GF-PDFs of the aged and continental aerosols also contain, besides the most hygroscopic background mode, particles with GFs between ∼ 1–1.4 (Fig. 12e, f), which are most likely a mixture of particles from local and regional origin with varying atmospheric age.

The GF-PDFs of the traffic influenced aerosol (Fig. 12b, f) contain a distinct non-hygroscopic mode peaking at GF between 0.9 and 1.05, which contains 18 % and 38 % of the particles at $D_0 = 265$ and 110 nm, respectively. This clearly indicates that the fresh traffic emissions are non-hygroscopic, consistent with diesel engine emission measurements by, e.g. Tritscher et al. (2011) or field measurements by Baltensperger et al. (2002), and that their relative contribution to the total particle number increases with decreasing particle size. A minor fraction of particles with GF between ∼ 1.1–1.4 is also present, as for the previously described aged and continental air masses. Particles with GF between ∼ 1.8–2 are also seen in the 75th percentiles in Fig. 12c, possibly indicating a short time period with influence from sea salt or de-icing salt.

The GF–PDF of the biomass burning influenced aerosol is, at $D_0 = 265$ nm (Fig. 12d), a mixture of freshly emitted slightly hygroscopic particles (peaking at GF ≈ 1.1) and more-hygroscopic background particles. A feature of the biomass burning influence is that the mode of freshly emitted particles is slightly more hygroscopic compared to the traffic influence. Results for $D_0 = 110$ nm are similar, except for a vanishing contribution of the more-hygroscopic background mode and a broader and slightly more hygroscopic fresh emissions mode (peaking between GF ≈ 1.15–1.3). These observations are consistent with variable but moderate hygroscopicity of fresh biomass burning emissions from different sources (e.g. Petters et al., 2009; Engelhart et al., 2012; Martin et al., 2012). Condensation of secondary organic and inorganic matter on the primary particles in the concentrated biomass burning plume may also contribute to slightly larger GFs at smaller dry sizes.

The relative importance of fresh emissions compared to the background aerosol generally increases with decreasing particle size. Total particle number is dominated by smaller particles, whereas total particle mass is dominated by larger particles. Consequently the local emissions have a stronger impact on particle number than on particle mass. It is important to account for this fact when judging the relevance of local emissions for aerosol impacts, which can either depend on particle number or on particle mass.

3.4 Hygroscopicity and mixing state of the BC particles

The GF-PDFs discussed in Sect. 3.3.5 revealed an external mixture of the urban aerosol with a non- or slightly hygroscopic mode, which is commonly attributed to fresh combustion emissions (Swietlicki et al., 2008), and a more hygroscopic mode formed by the background aerosol. The HTDMA alone can detect an external mixture of components with different hygroscopicity, however, an external mixture of components with similar hygroscopicity remain unresolved. In order to investigate the hygroscopic properties and mixing state of BC particles in detail, the SP2 has been coupled in series with the HTDMA (see Sect. 2 and Fig. 2) for a short period of time on 30–31 January 2010. By coincidence this short period contained the strongest biomass burning influence of the whole campaign according to the AAC (Fig. 3), also confirmed by a high BBOA mass fraction (not shown). This is reflected in a dominant mode of slightly hygroscopic particles peaking at a GF of ~ 1.1–1.2 between 30 January 08:00 p.m. LT and 31 January 07:00 a.m. LT (Fig. 13). A dominant influence of background aerosol, characterised by a dominance of the more-hygroscopic mode and a high OOA mass fraction, was also covered by this coupled measurement on 30 January between 3 a.m. and 6 p.m. The results shown in Fig. 14 from the coupled HTDMA-SP2 measurements were separately averaged for these two periods, in the following referred to as “background aerosol” and “biomass burning influence”.

The main difference between the averaged GF-PDFs of the “background aerosol” and the “biomass burning influence” is the relative abundance of more and slightly hygroscopic particles (blue shading in Fig. 14a, b). The SP2 reveals that most BC-containing particles (black shading) are found in the slightly hygroscopic mode. Furthermore, the slightly hygroscopic mode is an external mixture of particles with and without detectable BC core and most BC cores are found at GFs below ~ 1.1. Most more-hygroscopic particles do not contain a detectable BC core. Figure 14c, d shows the number fraction of BC particles as a function of particle hygroscopicity. Very similar results are found for both "background aerosols" and "biomass burning influence": essentially every non-hygroscopic particle with a GF of ~ 1.0 contains a BC core, while the number fraction of BC particles drops sharply to ~ 10–30 % for GF $\gtrsim$1.1. This result is consistent with a sharp increase of BC-containing particles at GF $\lesssim 1.1$ observed in urban Zurich (Switzerland) by Herich et al. (2008), who operated an ATOFMS in series with a HTDMA. However, McMeeking et al. (2011a), who conducted coupled HTDMA-SP2 measurements in urban Manchester (UK), observed that every particle in the mode with GF $\lesssim 1.2$, representing the fresh emission, contains a BC core. This discrepancy can be explained by the fact that diesel emissions are likely the only source of large particles in Manchester during summer time, while during winter time in Paris, the mode representing the fresh emission also contains organic-rich, slightly hygroscopic particles without a detectable BC core from biomass burning emissions. Figure 14 only shows the results for $D_0 = 265$ nm. Almost equal results with respect to external mixing of the slightly hygroscopic mode and the number fraction of BC cores as a function of the hygroscopic growth factor were also observed for $D_0 = 165$ and 110 nm.

The mixing state of the BC particles is further investigated by analysing the mean coating thickness as a function of the hygroscopic growth factor (Fig. 14e, f). The coloured lines indicate the theoretical relationship between coating thickness and hygroscopic factor for two-component particles with a total diameter of 265 nm that contain an insoluble BC core of variable size and a soluble coating with a certain κ value (see Sect. 2.4). The measured coating thickness (round markers) was derived from the SP2 data as explained in Sect. 2.1.3. The non-hygroscopic particles with GF $\lesssim 1.1$ have a negligible coating, which is consistent with fresh BC particles from traffic emissions (see also Figs. 6c and 10). The coating thickness sharply increases up to ~ 40–50 nm at GF = 1.15. These BC particles can most likely be attributed to biomass burning emissions, as the biomass burning emissions peak at this GF (see Fig. 6d), and as the coating thickness is consistent with a κ-value of ~ 0.1 of the coating, which is reasonable for BBOA (Martin et al., 2012). At GFs above 1.2, the coating thickness remains almost constant (for the biomass burning influence) or increases just slightly with increasing GF (for the background aerosol), but still much flatter than the coloured lines. This indicates that BC-containing particles in the GF range 1.2–1.6 mainly differ by the chemical composition (κ-value) of the coating rather than the coating thickness.

The external mixture of the slightly hygroscopic mode during the biomass burning influence is an important fact for the interpretation of the impact of biomass burning emissions on BC and total aerosol mass. The biomass burning emissions have a strong influence on the total aerosol mass, which is reflected in the dominant slightly hygroscopic mode (Fig. 14b), and thus the BBOA also contributes substantially to the total aerosol mass averaged over the whole campaign (Crippa et al., 2012). However, only a minor fraction of these slightly hygroscopic particles contains detectable amounts of BC. Furthermore, distinct biomass burning influence was only observed during part of the time, such that traffic is the major contributor to BC mass on average in agreement with the results from the bilinear regression model (Sect. 3.1) and the analysis of the diurnal patterns (Sect. 3.2).

The hygroscopic growth factor of a particle is related to the critical supersaturation required for CCN activation through Köhler theory. Figure 14g and h, which are identical, show this relationship for particles of different dry sizes. The curves are theoretically calculated using the single-parameter κ-Köhler theory and assuming surface tension of pure water (see Sect. 2.4). Jurányi et al. (2012) independently showed, by operating a CCN counter downstream of the HTDMA, that the actual hygroscopic behaviour of the Paris aerosol agrees, within experimental uncertainties, with the curves shown in Fig. 14g and h. A distinct feature of the Köhler curves is that the critical supersaturation increases sharply close to GF unity. The results presented in Fig. 14a–d show that the dominant fraction of the BC particles are non- or slightly hygroscopic. Consequently they require a substantially higher supersaturation for CCN activation compared to the majority of particles of equal dry size. It can therefore be expected that BC particles are enriched in the interstitial phase of liquid clouds. Size-resolved CCN measurements showed indeed that a minor fraction of the aerosol, in polluted environments, likely BC particles, remains inactivated at rather large diameters and high supersaturations (Rose et al., 2011). This composition specific activation behaviour is important to be considered in global simulations modelling atmospheric BC, as the wet scavenging efficiency remains a major source of uncertainty (Vignati et al., 2010).

4 Conclusions

The aerosol hygroscopicity and the BC properties were characterised for different sources and air mass origin in Paris, one of the biggest European megacities.

The growth factor distributions, characterised by distinct modes of more-hygroscopic background aerosol and non- or slightly hygroscopic aerosol of local (or regional) origin, revealed an increase of the relative contribution of the local sources compared to the background aerosol with decreasing particle size. Different approaches to identify the sources of the particulate BC mass in Paris indicate a dominant influence from traffic emissions, whereas biomass burning only presents a minor contribution. The mass size distribution of the BC cores peaked on average at a BC core mass equivalent diameter of $D_{\mathrm{MEV}} \approx 150\,\mathrm{nm}$. The BC particles were moderately coated ($\Delta_{\mathrm{coat}} \approx 30\,\mathrm{nm}$ on average for BC cores with $D_{\mathrm{MEV}} = 200\,\mathrm{nm}$) and a MAC of $\sim 8.6\ \mathrm{m^2\,g^{-1}}$ at $\lambda = 880\,\mathrm{nm}$ was observed on average. However, distinct differences of aerosol and BC properties were observed between different air mass types.

The traffic emissions were found to be non-hygroscopic ($\mathrm{GF} \approx 1.0$ at $\mathrm{RH} = 90\,\%$), and essentially all particles with a diameter larger than 110 nm contained a BC core. BC from traffic emissions was further characterised by literally no coating ($\Delta_{\mathrm{coat}} \approx 2\,\mathrm{nm}$), the smallest maximum of the BC core mass size distribution ($D_{\mathrm{MEV}} \approx 100\,\mathrm{nm}$) and the smallest MAC ($\sim 7.3\,\mathrm{m^2\,g^{-1}}$ at $\lambda = 880\,\mathrm{nm}$). The biomass burning aerosol, characterised by a distinct slightly hygroscopic mode peaking at GF ≈ 1.1–1.2, was slightly more hygroscopic than the traffic emissions. Furthermore, only a minor fraction ($\leqslant 10\,\%$) of the slightly hygroscopic particles with GF $\geqslant 1.1$ (with a $D_0 = 265\,\mathrm{nm}$) contained a detectable BC core. This indicates that the impact of biomass burning emissions is relatively more important for total aerosol mass than for BC mass. The BC particles from biomass burning were found to have a medium coating thickness as well as slightly larger mean core sizes and MAC values compared to traffic emissions.

The aerosol observed under the influence of aged air masses and air masses from Eastern Continental Europe was dominated by a more hygroscopic mode peaking at GF(90 % RH) ≈ 1.6. 95 % of the particles (with a $D_0 = 265\,\mathrm{nm}$) in the background mode did not contain a detectable BC core. A significant fraction of the BC particles, except those from local emissions, which are also present, had a substantial coating with non-refractory aerosol components. MAC values of $\sim 8.8\,\mathrm{m^2\,g^{-1}}$ at $\lambda = 880$ and $\sim 8.3\,\mathrm{m^2\,g^{-1}}$ at $\lambda = 880\,\mathrm{nm}$ and mass mean BC core diameters of 150 nm and 200 nm were observed for the aged and continental air mass types. The reason for the larger BC core sizes compared to the fresh emissions – transport effects or a different BC source – remains unclear.

On average the dominant fraction of the BC particles were found to be non- or slightly hygroscopic. Consequently they require a higher supersaturation for CCN activation compared to the majority of particles of equal dry size. It can therefore be expected that BC particles are enriched in the interstitial phase of liquid clouds, thereby decreasing their wet removal efficiency. This composition specific activation behaviour is important to be considered in global simulations modelling atmospheric BC, as the wet scavenging efficiency remains a major source of uncertainty.

Acknowledgements. This research in the context of the MEGAPOLI project is mainly financially supported by the European Community's Framework Program FP/2007-2011 under grant agreement no 212520 and the Swiss National Science Foundation. SIRTA, LHVP are particularly thanked for their strong support in the field.

References

Baltensperger, U., Streit, N., Weingartner, E., Nyeki, S., Prévôt, A. S. H., Van Dingenen, R., Virkkula, A., Putaud, J. P., Even, A., Brink, H. T., Blatter, A., Neftel, A., and Gäggeler, H. W.: Urban and rural aerosol characterization of summer smog events during the PIPAPO field campaign in Milan, Italy, J. Geophys. Res., 107, 8193, doi:10.1029/2001JD001292, 2002. 25142, 25150

Baumgardner, D., Popovicheva, O., Allan, J., Bernardoni, V., Cao, J., Cavalli, F., Cozic, J., Diapouli, E., Eleftheriadis, K., Genberg, P. J., Gonzalez, C., Gysel, M., John, A., Kirchstetter, T. W., Kuhlbusch, T. A. J., Laborde, M., Lack, D., Müller, T., Niessner, R., Petzold, A., Piazzalunga, A., Putaud, J. P., Schwarz, J., Sheridan, P., Subramanian, R., Swietlicki, E., Valli, G., Vecchi, R., and Viana, M.: Soot reference materials for instrument calibration and intercomparisons: a workshop summary with recommendations, Atmos. Meas. Tech., 5, 1869–1887, doi:10.5194/amt-5-1869-2012, 2012. 25127, 25128

Beekmann, M., Prévôt, A. S. H., Drewnick, F., Sciare, J., Pandis, S. N., van der Gon, H. A. C. D., Crippa, M., Freutel, F., Poulain, L., Ghersi, V., Rodriguez, E., Beirle, S., Zotter, P., von der Weiden-Reinmüller, S.-L., Bressi, M., Fountoukis, C., Petetin, H., Szidat, S., Schneider, J., Rossi, A., Haddad, I. E., Megaritis, A., Zhang, Q. J., Slowik, J. G., Moukthar, S., Kolmonen, P., Stohl, A., Eckhardt, S., Borbon, A., Gros, V., Marchand, N., Jaffrezo, J. L., Schwarzenboeck, A., Colomb, A., Wiedensohler, A., Borrmann, S., Lawrence, M., Baklanov, A., and Baltensperger, U.: Air pollution in a European megacity: the origin of fine particulate matter, submitted to Proc. Natl Acad. Sci., 2012. 25138

Bond, T. C. and Bergstrom, R. W.: Light absorption by carbonaceous particles: an investigative review, Aerosol Sci. Technol., 40, 27–67, 2006. 25148, 25149

Cheng, Y. F., Berghof, M., Garland, R. M., Wiedensohler, A., Wehner, B., Müller, T., Su, H., Zhang, Y. H., Achtert, P., Nowak, A., Pöschl, U., Zhu, T., Hu, M., and Zeng, L. M.: Influence of soot mixing state on aerosol light absorption and single scattering albedo during air mass aging at a polluted regional site in Northeastern China, J. Geophys. Res., 114, D00G10, doi:10.1029/2008jd010883, 2009. 25126

Chirico, R., DeCarlo, P. F., Heringa, M. F., Tritscher, T., Richter, R., Prévôt, A. S. H., Dommen, J., Weingartner, E., Wehrle, G., Gysel, M., Laborde, M., and Baltensperger, U.: Impact of aftertreatment devices on primary emissions and secondary organic aerosol formation potential from in-use diesel vehicles: results from smog chamber experiments, Atmos. Chem. Phys., 10, 11545–11563, doi:10.5194/acp-10-11545-2010, 2010. 25124, 25146

Chung, S. H. and Seinfeld, J. H.: Global distribution and climate forcing of carbonaceous aerosols, J. Geophys. Res., 107, 4407, doi:10.1029/2001JD001397, 2002. 25123

Cozic, J., Verheggen, B., Mertes, S., Connolly, P., Bower, K., Petzold, A., Baltensperger, U., and Weingartner, E.: Scavenging of black carbon in mixed phase clouds at the high alpine site Jungfraujoch, Atmos. Chem. Phys., 7, 1797–1807, doi:10.5194/acp-7-1797-2007, 2007. 25124

Crippa, M., DeCarlo, P. F., Slowik, J. G., Mohr, C., Heringa, M., F., Chirico, R., Poulain, L., Freutel, F., Sciare, J., Cozic, J., Di Marco, C. F., Elsässer, M., José, N., Marchand, N., Abidi, E., Wiedensohler, A., Drewnick, F., Schneider, J., Borrmann, S., Nemitz, E., Zimmermann, R., Jaffrezo, J.-L., Prévôt, A. S. H., and Baltensperger, U.: Wintertime aerosol chemical composition and source apportionment of the organic fraction in the metropolitan area of Paris, Atmos. Chem. Phys. Discuss., 12, 22535–22586, doi:10.5194/acpd-12-22535-2012, 2012. 25131, 25139, 25141, 25153

DeCarlo, P. F., Slowik, J. G., Worsnop, D. R., Davidovits, P., and Jimenez, J. L.: Particle morphology and density characterization by combined mobility and aerodynamic diameter measurements. Part 1: theory, Aerosol Sci. Technol., 39, 184, 2004. 25124

DeCarlo, P. F., Kimmel, J. R., Trimborn, A., Northway, M. J., Jayne, J. T., Aiken, A. C., Gonin, M., Fuhrer, K., Horvath, T., Docherty, K. S., Worsnop, D. R., and Jimenez, J. L.: Field-deployable, high-resolution, time-of-flight aerosol mass spectrometer, Anal. Chem., 78, 8281–8289, 2006. 25131

DeMott, P. J., Chen, Y., Kreidenweis, S. M., Rogers, D. C., and Sherman, D. E.: Ice formation by black carbon particles, Geophys. Res. Lett., 26, 2429–2432, doi:10.1029/1999GL900580, 1999. 25123

Dusek, U., Frank, G. P., Hildebrandt, L., Curtius, J., Schneider, J., Walter, S., Chand, D., Drewnick, F., Hings, S., Jung, D., Borrmann, S., and Andreae, M. O.: Size matters more than chemistry for cloud-nucleating ability of aerosol particles, Science, 312, 1375–1378, 2006. 25124

Engelhart, G. J., Hennigan, C. J., Miracolo, M. A., Robinson, A. L., and Pandis, S. N.: Cloud condensation nuclei activity of fresh primary and aged biomass burning aerosol, Atmos. Chem. Phys., 12, 7285–7293, doi:10.5194/acp-12-7285-2012, 2012. 25150

Gao, R. S., Schwarz, J. P., Kelly, K. K., Fahey, D. W., Watts, L. A., Thompson, T. L., Spackman, J. R., Slowik, J. G., Cross, E. S., Han, J. H., Davidovits, P., Onasch, T. B., and Worsnop, D. R.: A novel method for estimating light-scattering properties of soot aerosols using a modified single-particle soot photometer, Aerosol Sci. Technol., 41, 125–135, 2007. 25128

Gysel, M., Crosier, J., Topping, D. O., Whitehead, J. D., Bower, K. N., Cubison, M. J., Williams, P. I., Flynn, M. J., McFiggans, G. B., and Coe, H.: Closure study between chemical composition and hygroscopic growth of aerosol particles during TORCH2, Atmos. Chem. Phys., 7, 6131–6144, doi:10.5194/acp-7-6131-2007, 2007. 25133

Gysel, M., McFiggans, G. B., and Coe, H.: Inversion of tandem differential mobility analyser (TDMA) measurements, J. Aerosol. Sci., 40, 134–151, 2009. 25130

Gysel, M., Laborde, M., Olfert, J. S., Subramanian, R., and Gröhn, A. J.: Effective density of Aquadag and fullerene soot black carbon reference materials used for SP2 calibration, Atmos. Meas. Tech., 4, 2851–2858, doi:10.5194/amt-4-2851-2011, 2011. 25127, 25128

Haeffelin, M., Barthès, L., Bock, O., Boitel, C., Bony, S., Bouniol, D., Chepfer, H., Chiriaco, M., Cuesta, J., Delanoë, J., Drobinski, P., Dufresne, J.-L., Flamant, C., Grall, M., Hodzic, A., Hourdin, F., Lapouge, F., Lemaître, Y., Mathieu, A., Morille, Y., Naud, C., Noël, V., O'Hirok, W., Pelon, J., Pietras, C., Protat, A., Romand, B., Scialom, G., and Vautard, R.: SIRTA, a ground-based atmospheric observatory for cloud and aerosol research, Ann. Geophys., 23, 253–275, doi:10.5194/angeo-23-253-2005, 2005. 25134

Healy, R. M., Sciare, J., Poulain, L., Kamili, K., Merkel, M., Müller, T., Wiedensohler, A., Eckhardt, S., Stohl, A., Sarda-Estève, R., McGillicuddy, E., O'Connor, I. P., Sodeau, J. R., and Wenger, J. C.: Sources and mixing state of size-resolved elemental carbon particles in a European megacity: Paris, Atmos. Chem. Phys., 12, 1681–1700, doi:10.5194/acp-12-1681-2012, 2012. 25124, 25126, 25141, 25144, 25145

Hennigan, C. J., Miracolo, M. A., Engelhart, G. J., May, A. A., Presto, A. A., Lee, T., Sullivan, A. P., McMeeking, G. R., Coe, H., Wold, C. E., Hao, W.-M., Gilman, J. B., Kuster, W. C., de Gouw, J., Schichtel, B. A., J. L. Collett Jr., Kreidenweis, S. M., and Robinson, A. L.: Chemical and physical transformations of organic aerosol from the photo-oxidation of open biomass burning emissions in an environmental chamber, Atmos. Chem. Phys., 11, 7669–7686, doi:10.5194/acp-11-7669-2011, 2011. 25147

Herich, H., Kammermann, L., Gysel, M., Weingartner, E., Baltensperger, U., Lohmann, U., and Cziczo, D. J.: In situ determination of atmospheric aerosol composition as a function of hygroscopic growth, J. Geophys. Res., 113, D16213, doi:10.1029/2008JD009954, 2008. 25125, 25152

Heringa, M. F., DeCarlo, P. F., Chirico, R., Tritscher, T., Dommen, J., Weingartner, E., Richter, R., Wehrle, G., Prévôt, A. S. H., and Baltensperger, U.: Investigations of primary and secondary particulate matter of different wood combustion appliances with a high-resolution time-of-flight aerosol mass spectrometer, Atmos. Chem. Phys., 11, 5945–5957, doi:10.5194/acp-11-5945-2011, 2011. 25124, 25147

Hoque, R. R., Khillare, P. S., Agarwal, T., Shridhar, V., and Balachandran, S.: Spatial and temporal variation of BTEX in the urban atmosphere of Delhi, India, Sci. Total Environ., 392, 30–40, 2008. 25138

Invernizzi, G., Ruprecht, A., Mazza, R., De Marco, C., Mocnik, G., Sioutas, C., and Westerdahl, D.: Measurement of black carbon concentration as an indicator of air quality benefits of traffic restriction policies within the Ecopass zone in Milan, Italy, Atmos. Environ., 45, 3522–3527, 2011. 25135, 25137

Jacobson, M. Z.: Strong radiative heating due to the mixing state of black carbon in atmospheric aerosols, Nature, 409, 695–697, 2001. 25123

Jurányi, Z., Gysel, M., Tritscher, T., Weingartner, E., Laborde, M., and Baltensperger, U.: Hygroscipicity mixing state closure from Paris, to be submitted to Atmos. Chem. Phys. Discuss., 2012. 25124, 25153

Khoder, M. I.: Ambient levels of volatile organic compounds in the atmosphere of greater Cairo, Atmos. Environ., 41, 554–566, 2007. 25138

Koch, D., Schulz, M., Kinne, S., McNaughton, C., Spackman, J. R., Balkanski, Y., Bauer, S., Berntsen, T., Bond, T. C., Boucher, O., Chin, M., Clarke, A., De Luca, N., Dentener, F., Diehl, T., Dubovik, O., Easter, R., Fahey, D. W., Feichter, J., Fillmore, D., Freitag, S., Ghan, S., Ginoux, P., Gong, S., Horowitz, L., Iversen, T., Kirkevåg, A., Klimont, Z., Kondo, Y., Krol, M., Liu, X., Miller, R., Montanaro, V., Moteki, N., Myhre, G., Penner, J. E., Perlwitz, J., Pitari, G., Reddy, S., Sahu, L., Sakamoto, H., Schuster, G., Schwarz, J. P., Seland, Ø., Stier, P., Takegawa, N., Takemura, T., Textor, C., van Aardenne, J. A., and Zhao, Y.: Corrigendum to "Evaluation of black carbon estimations in global aerosol models" published in Atmos. Chem. Phys., 9, 9001–9026, 2009, Atmos. Chem. Phys., 10, 79–81, doi:10.5194/acp-10-79-2010, 2010. 25123

Kondo, Y., Sahu, L., Moteki, N., Khan, F., Takegawa, N., Liu, X., Koike, M., and Miyakawa, T.: Consistency and traceability of black carbon measurements made by laser-induced incandescence, thermal-optical transmittance, and filter-based photo-absorption techniques, Aerosol Sci. Technol., 45, 295–312, 2011. 25127

Kuwata, M. and Kondo, Y.: Dependence of size-resolved CCN spectra on the mixing state of nonvolatile cores observed in Tokyo, J. Geophys. Res., 113, D19202, doi:10.1029/2007JD009761, 2008. 25124, 25125

Laborde, M., Mertes, P., Zieger, P., Dommen, J., Baltensperger, U., and Gysel, M.: Sensitivity of the Single Particle Soot Photometer to different black carbon types, Atmos. Meas. Tech., 5, 1031–1043, doi:10.5194/amt-5-1031-2012, 2012a. 25127

Laborde, M., Schnaiter, M., Linke, C., Saathoff, H., Naumann, K.-H., Möhler, O., Berlenz, S., Wagner, U., Taylor, J. W., Liu, D., Flynn, M., Allan, J. D., Coe, H., Heimerl, K., Dahlkötter, F., Weinzierl, B., Wollny, A. G., Zanatta, M., Cozic, J., Laj, P., Hitzenberger, R., Schwarz, J. P., and Gysel, M.: Single Particle Soot Photometer intercomparison at the AIDA chamber, Atmos. Meas. Tech. Discuss., 5, 3519–3573, doi:10.5194/amtd-5-3519-2012, 2012b. 25127, 25128, 25129

Lindinger, W., Hansel, A., and Jordan, A.: On-line monitoring of volatile organic compounds at pptv levels by means of proton-transfer-reaction mass spectrometry (PTR-MS) – medical applications, food control and environmental research, Int. J. Mass Spectrom., 173, 191–241, 1998. 25132

Liousse, C. and Cachier, H.: Measurement of black carbon aerosols in the atmosphere of 2 different source regions – real-time data for the Paris region and a Savanna site of the Ivory-Coast, Environ. Technol., 13, 959–967, 1992. 25126

Liu, D., Allan, J., Corris, B., Flynn, M., Andrews, E., Ogren, J., Beswick, K., Bower, K., Burgess, R., Choularton, T., Dorsey, J., Morgan, W., Williams, P. I., and Coe, H.: Carbonaceous aerosols contributed by traffic and solid fuel burning at a polluted rural site in Northwestern England, Atmos. Chem. Phys., 11, 1603–1619, doi:10.5194/acp-11-1603-2011, 2011. 25141

Martin, M., Tritscher, T., Jurányi, Z., Heringa, M. F., Sierau, B., Weingartner, E., Chirico, R., Gysel, M., Prévôt, A. S. H., Baltensperger, U., and Lohmann, U.: Hygroscopicity properties of fresh and aged wood burning particles, J. Aerosol. Sci., in press, doi:10.1016/j.jaerosci.2012.08.006, 2012. 25150, 25153

McFiggans, G., Artaxo, P., Baltensperger, U., Coe, H., Facchini, M. C., Feingold, G., Fuzzi, S., Gysel, M., Laaksonen, A., Lohmann, U., Mentel, T. F., Murphy, D. M., O'Dowd, C. D., Snider, J. R., and Weingartner, E.: The effect of physical and chemical aerosol properties on warm cloud droplet activation, Atmos. Chem. Phys., 6, 2593–2649, doi:10.5194/acp-6-2593-2006, 2006. 25133

McMeeking, G. R., Good, N., Petters, M. D., McFiggans, G., and Coe, H.: Influences on the fraction of hydrophobic and hydrophilic black carbon in the atmosphere, Atmos. Chem. Phys., 11, 5099–5112, doi:10.5194/acp-11-5099-2011, 2011a. 25125, 25152

McMeeking, G. R., Morgan, W. T., Flynn, M., Highwood, E. J., Turnbull, K., Haywood, J., and Coe, H.: Black carbon aerosol mixing state, organic aerosols and aerosol optical properties over the United Kingdom, Atmos. Chem. Phys., 11, 9037–9052, doi:10.5194/acp-11-9037-2011, 2011b. 25126

Moosmüller, H., Chakrabarty, R. K., Ehlers, K. M., and Arnott, W. P.: Absorption Ångström coefficient, brown carbon, and aerosols: basic concepts, bulk matter, and spherical particles, Atmos. Chem. Phys., 11, 1217–1225, doi:10.5194/acp-11-1217-2011, 2011. 25138

Moteki, N. and Kondo, Y.: Effects of mixing state on black carbon measurements by laser-induced incandescence, Aerosol Sci. Technol., 41, 398–417, 2007. 25127

Moteki, N. and Kondo, Y.: Dependence of laser-induced incandescence on physical properties of black carbon aerosols: measurements and theoretical interpretation, Aerosol Sci. Technol., 44, 663–675, 2010. 25127

Moteki, N., Kondo, Y., and Nakamura, S.: Method to measure refractive indices of small non-spherical particles: application to black carbon particles, J. Aerosol. Sci., 41, 513–521, 2010. 25129

Moteki, N., Kondo, Y., Oshima, N., Takegawa, N., Koike, M., Kita, K., Matsui, H., and Kajino, M.: Size dependence of wet removal of black carbon aerosols during transport from the boundary layer to the free troposphere, Geophys. Res. Lett., 39, L13802, doi:10.1029/2012GL052034, 2012. 25145

Nakayama, T., Matsumi, Y., Sato, K., Imamura, T., Yamazaki, A., and Uchiyama, A.: Laboratory studies on optical properties of secondary organic aerosols generated during the photooxidation of toluene and the ozonolysis of α-pinene, J. Geophys. Res., 115, D24204, doi:10.1029/2010JD014387, 2010. 25129

Petters, M. D. and Kreidenweis, S. M.: A single parameter representation of hygroscopic growth and cloud condensation nucleus activity, Atmos. Chem. Phys., 7, 1961–1971, doi:10.5194/acp-7-1961-2007, 2007. 25133, 25134

Petters, M. D., Carrico, C. M., Kreidenweis, S. M., Prenni, A. J., DeMott, P. J., Collett, J. L. J., and Moosmüller, H.: Cloud condensation nucleation activity of biomass burning aerosol, J. Geophys. Res., 114, D22205, doi:10.1029/2009JD012353, 2009. 25150

Querol, X., Pey, J., Minguillón, M. C., Pérez, N., Alastuey, A., Viana, M., Moreno, T., Bernabé, R. M., Blanco, S., Cárdenas, B., Vega, E., Sosa, G., Escalona, S., Ruiz, H., and Artíñano, B.: PM speciation and sources in Mexico during the MILAGRO-2006 Campaign, Atmos. Chem. Phys., 8, 111–128, doi:10.5194/acp-8-111-2008, 2008. 25137

Ramanathan, V. and Carmichael, G.: Global and regional climate changes due to black carbon, Nat. Geosci., 1, 221–227, 2008. 25123

Reche, C., Querol, X., Alastuey, A., Viana, M., Pey, J., Moreno, T., Rodríguez, S., González, Y., Fernández-Camacho, R., de la Rosa, J., Dall'Osto, M., Prévôt, A. S. H., Hueglin, C., Harrison, R. M., and Quincey, P.: New considerations for PM, Black Carbon and particle number concentration for air quality monitoring across different European cities, Atmos. Chem. Phys., 11, 6207–6227, doi:10.5194/acp-11-6207-2011, 2011. 25135, 25137

Rose, D., Gunthe, S. S., Su, H., Garland, R. M., Yang, H., Berghof, M., Cheng, Y. F., Wehner, B., Achtert, P., Nowak, A., Wiedensohler, A., Takegawa, N., Kondo, Y., Hu, M., Zhang, Y., Andreae, M. O., and Pöschl, U.: Cloud condensation nuclei in polluted air and biomass burning smoke near the mega-city Guangzhou, China – Part 2: Size-resolved aerosol chemical composition, diurnal cycles, and externally mixed weakly CCN-active soot particles, Atmos. Chem. Phys., 11, 2817–2836, doi:10.5194/acp-11-2817-2011, 2011. 25124, 25149, 25154

Ruellan, S. and Cachier, H.: Characterisation of fresh particulate vehicular exhausts near a Paris high flow road, Atmos. Environ., 35, 453–468, 2001. 25126

Sandradewi, J., Prévôt, A. S. H., Weingartner, E., Schmidhauser, R., Gysel, M., and Baltensperger, U.: A study of wood burning and traffic aerosols in an Alpine valley using a multi-wavelength aethalometer, Atmos. Environ., 42, 101–112, 2008. 25139, 25141

Schnaiter, M., Horvath, H., Möhler, O., Naumann, K. H., Saathoff, H., and Schock, O. W.: UV-VIS-NIR spectral optical properties of soot and soot-containing aerosols, J. Aerosol. Sci., 34, 1421–1444, 2003. 25129

Schnaiter, M., Linke, C., Möhler, O., Naumann, K. H., Saathoff, H., Wagner, R., Schurath, U., and Wehner, B.: Absorption amplification of black carbon internally mixed with secondary organic aerosol, J. Geophys. Res. Atmos., 110, D19204, doi:10.1029/2005JD006046, 2005. 25124, 25148

Schwarz, J. P., Gao, R. S., Fahey, D. W., Thomson, D. S., Watts, L. A., Wilson, J. C., Reeves, J. M., Darbeheshti, M., Baumgardner, D. G., Kok, G. L., Chung, S. H., Schulz, M., Hendricks, J., Lauer, A., Karcher, B., Slowik, J. G., Rosenlof, K. H., Thompson, T. L., Langford, A. O., Loewenstein, M., and Aikin, K. C.: Single-particle measurements of midlatitude black carbon and light-scattering aerosols from the boundary layer to the lower stratosphere, J. Geophys. Res., 111, D16207, doi:10.1029/2006JD007076, 2006. 25126

Schwarz, J. P., Gao, R. S., Spackman, J. R., Watts, L. A., Thomson, D. S., Fahey, D. W., Ryerson, T. B., Peischl, J., Holloway, J. S., Trainer, M., Frost, G. J., Baynard, T., Lack, D. A., de Gouw, J. A., Warneke, C., and Del Negro, L. A.: Measurement of the mixing state, mass, and optical size of individual black carbon particles in urban and biomass burning emissions, Geophys. Res. Lett., 35, L13810, doi:10.1029/2008GL033968, 2008a. 25125, 25136, 25144, 25146, 25147

Schwarz, J. P., Spackman, J. R., Fahey, D. W., Gao, R. S., Lohmann, U., Stier, P., Watts, L. A., Thomson, D. S., Lack, D. A., Pfister, L., Mahoney, M. J., Baumgardner, D., Wilson, J. C., and Reeves, J. M.: Coatings and their enhancement of black carbon light absorption in the tropical atmosphere, J. Geophys. Res., 113, D03203, doi:10.1029/2007JD009042, 2008b. 25124, 25128

Sciare, J., d'Argouges, O., Zhang, Q. J., Sarda-Estève, R., Gaimoz, C., Gros, V., Beekmann, M., and Sanchez, O.: Comparison between simulated and observed chemical composition of fine aerosols in Paris (France) during springtime: contribution of regional versus continental emissions, Atmos. Chem. Phys., 10, 11987–12004, doi:10.5194/acp-10-11987-2010, 2010. 25126

Shindell, D., Kuylenstierna, J. C. I., Vignati, E., van Dingenen, R., Amann, M., Klimont, Z., Anenberg, S. C., Muller, N., Janssens-Maenhout, G., Raes, F., Schwartz, J., Faluvegi, G., Pozzoli, L., Kupiainen, K., Höglund-Isaksson, L., Emberson, L., Streets, D., Ramanathan, V., Hicks, K., Oanh, N. T. K., Milly, G., Williams, M., Demkine, V., and Fowler, D.: Simultaneously mitigating near-term climate change and improving human health and food security, Science, 335, 183–189, 2012. 25123

Shiraiwa, M., Kondo, Y., Moteki, N., Takegawa, N., Sahu, L. K., Takami, A., Hatakeyama, S., Yonemura, S., and Blake, D. R.: Radiative impact of mixing state of black carbon aerosol in Asian outflow, J. Geophys. Res., 113, D24210, doi:10.1029/2008JD010546, 2008. 25125, 25126, 25136, 25145, 25146

Solomon, S.: Intergovernmental Panel on Climate Change, and Intergovernmental Panel on Climate Change. Working Group I.: Climate Change 2007: The Physical Science Basis: Contribution of Working Group I to the Fourth Assessment Report of the Intergovernmental Panel on Climate Change, Climate Change 2007, Cambridge University Press, Cambridge, 2007. 25123

Stephens, M., Turner, N., and Sandberg, J.: Particle identification by laser-induced incandescence in a solid-state laser cavity, Appl. Opt., 42, 3726–3736, 2003. 25125, 25126

Stohl, A., Hittenberger, M., and Wotawa, G.: Validation of the Lagrangian particle dispersion model FLEXPART against large-scale tracer experiment data, Atmos. Environ., 32, 4245–4264, doi:10.1016/S1352-2310(98)00184-8, 1998. 25132

Stohl, A., Forster, C., Frank, A., Seibert, P., and Wotawa, G.: Technical note: The Lagrangian particle dispersion model FLEXPART version 6.2, Atmos. Chem. Phys., 5, 2461–2474, doi:10.5194/acp-5-2461-2005, 2005. 25132

Subramanian, R., Kok, G. L., Baumgardner, D., Clarke, A., Shinozuka, Y., Campos, T. L., Heizer, C. G., Stephens, B. B., de Foy, B., Voss, P. B., and Zaveri, R. A.: Black carbon over Mexico: the effect of atmospheric transport on mixing state, mass absorption cross-section, and BC/CO ratios, Atmos. Chem. Phys., 10, 219–237, doi:10.5194/acp-10-219-2010, 2010. 25135, 25137

Sullivan, R. C. and Prather, K. A.: Recent advances in our understanding of atmospheric chemistry and climate made possible by on-line aerosol analysis instrumentation, Anal. Chem., 77, 3861–3885, 2005. 25124

Swietlicki, E., Hansson, H. C., Hämeri, K., Svenningsson, B., Massling, A., McFiggans, G., McMurry, P. H., Petäjä, T., Tunved, P., Gysel, M., Topping, D., Weingartner, E., Baltensperger, U., Rissler, J., Wiedensohler, A., and Kulmala, M.: Hygroscopic properties of submicrometer atmospheric aerosol particles measured with H-TDMA instruments in various environments – a review, Tellus, 60B, 432–469, 2008. 25124, 25150, 25151

Toon, O. B., Pollack, J. B., and Khare, B. N.: Optical-constants of several atmospheric aerosol species – ammonium-sulfate, aluminum-oxide, and sodium-chloride, J. Geophys. Res., 81, 5733–5748, 1976. 25129

Tritscher, T., Jurányi, Z., Martin, M., Chirico, R., Gysel, M., Heringa, M. F., DeCarlo, P. F., Sierau, B., Prévôt, A. S. H., Weingartner, E., and Baltensperger, U.: Changes of hygroscopicity and morphology during ageing of diesel soot, Environ. Res. Lett., 6, 034026, doi:10.1088/1748-9326/6/3/034026, 2011. 25124, 25130, 25150

Ulbrich, I. M., Canagaratna, M. R., Zhang, Q., Worsnop, D. R., and Jimenez, J. L.: Interpretation of organic components from Positive Matrix Factorization of aerosol mass spectrometric data, Atmos. Chem. Phys., 9, 2891–2918, doi:10.5194/acp-9-2891-2009, 2009. 25131

Vignati, E., Karl, M., Krol, M., Wilson, J., Stier, P., and Cavalli, F.: Sources of uncertainties in modelling black carbon at the global scale, Atmos. Chem. Phys., 10, 2595–2611, doi:10.5194/acp-10-2595-2010, 2010. 25123, 25154

Weingartner, E., Saathoff, H., Schnaiter, M., Streit, N., Bitnar, B., and Baltensperger, U.: Absorption of light by soot particles: determination of the absorption coefficient by means of aethalometers, J. Aerosol. Sci., 34, 1445–1463, 2003. 25131

Wiedensohler, A., Birmili, W., Nowak, A., Sonntag, A., Weinhold, K., Merkel, M., Wehner, B., Tuch, T., Pfeifer, S., Fiebig, M., Fjäraa, A. M., Asmi, E., Sellegri, K., Depuy, R., Venzac, H., Villani, P., Laj, P., Aalto, P., Ogren, J. A., Swietlicki, E., Williams, P., Roldin, P., Quincey, P., Hüglin, C., Fierz-Schmidhauser, R., Gysel, M., Weingartner, E., Riccobono, F., Santos, S., Grüning, C., Faloon, K., Beddows, D., Harrison, R., Monahan, C., Jennings, S. G., O'Dowd, C. D., Marinoni, A., Horn, H.-G., Keck, L., Jiang, J., Scheckman, J., McMurry, P. H., Deng, Z., Zhao, C. S., Moerman, M., Henzing, B., de Leeuw, G., Löschau, G., and Bastian, S.: Mobility particle size spectrometers: harmonization of technical standards and data structure to facilitate high quality long-term observations of atmospheric particle number size distributions, Atmos. Meas. Tech., 5, 657–685, doi:10.5194/amt-5-657-2012, 2012. 25132

Table 1. Averages of the coating thickness Δ_{coat} of non-refractory matter on BC cores with a mass equivalent diameter of ~200 nm and ~260 nm, the mass absorption coefficient (MAC) and the toluene to benzene mixing ratios (T/B) for each air mass type or aerosol source investigated and for the entire measurement campaign.

Air mass type/ aerosol source	T/B (–)	Δ_{coat} (nm) BC core ~200 nm	Δ_{coat} (nm) BC core ~260 nm	MAC $m^2\,g^{-1}$
Continental	1.21	76	93	8.3
Aged air mass	1.36	44	37	8.8
Biomass burning	2.27	15	11	7.8
Traffic	4.3	2	2	7.3
Entire dataset	2	32	35	8.6

Title Page
Abstract | Introduction
Conclusions | References
Tables | Figures
◀| |▶
◀ ▶
Back | Close
Full Screen / Esc
Printer-friendly Version
Interactive Discussion

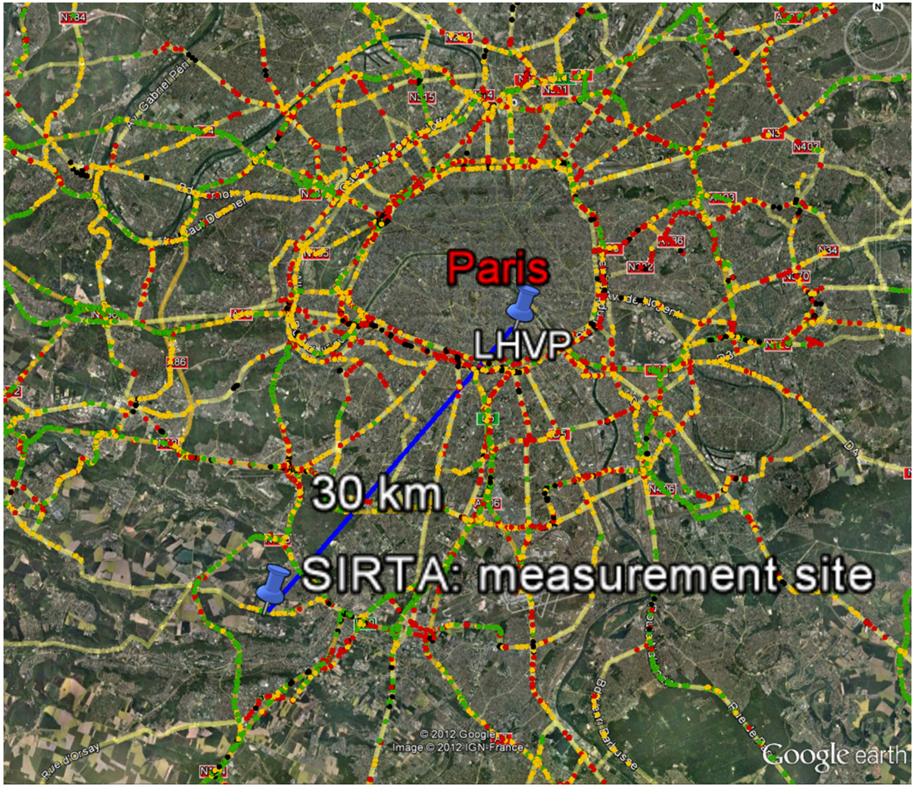

Fig. 1. SIRTA measurement platform, 30 km south-west of the other measurement station (LHVP), situated in Paris centre. The coloured dots represent the traffic on the principal highways around Paris (red and green dots indicate the highest and lowest traffic density, respectively).

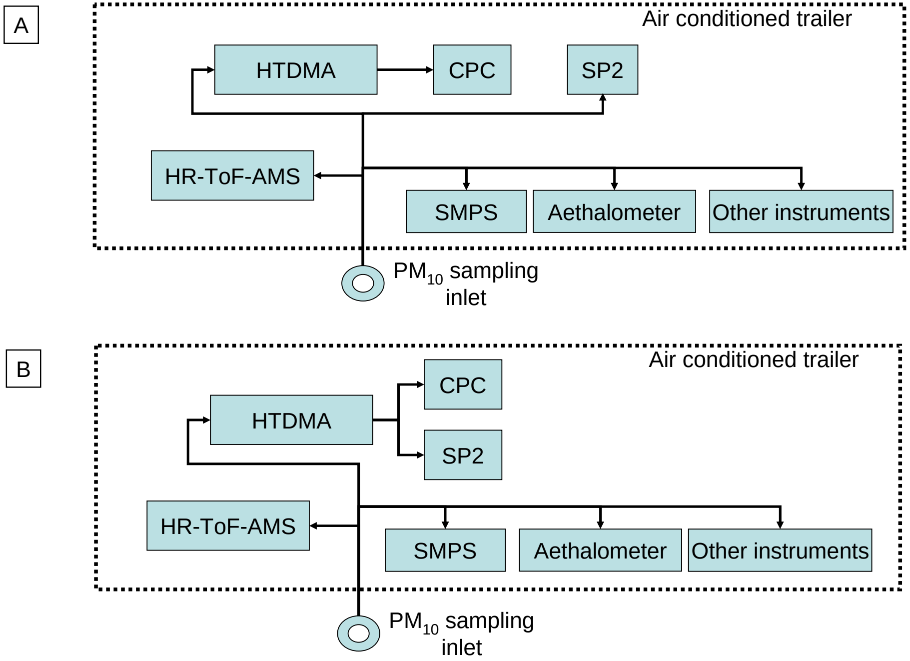

Fig. 2. Experimental setup during the majority of the measurement campaign **(A)** and during the period with coupled HTDMA-SP2 setup (**B**: 30–31 January).

Title Page
Abstract | Introduction
Conclusions | References
Tables | Figures
◀| |▶
◀ ▶
Back | Close
Full Screen / Esc
Printer-friendly Version
Interactive Discussion

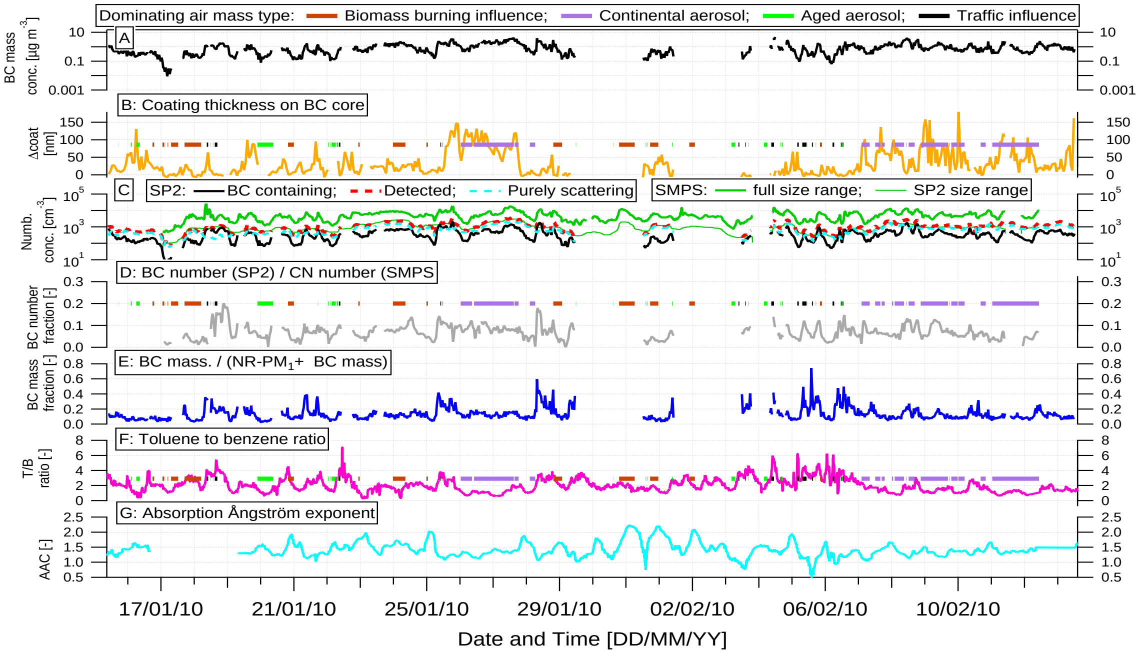

Fig. 3. Time series of **(A)** BC mass concentration (SP2) – **(B)** Median coating thickness of non-refractory material on BC cores with 180 nm ≤ D_{MEV} ≤ 220 nm (SP2) – **(C)** Number concentration of purely scattering (blue lines), BC-containing (black line) and total detected particles (red dashed line) as measured by the SP2. Number concentration of particles in the SMPS detection range (thick green line) and in the SP2 detection range (CN; thin green line) as measured by the SMPS – **(D)** BC number fraction (SP2), relative to the total number of particles (SMPS) – **(E)** BC mass fraction (SP2), relative to the sum of BC mass and non refractory PM_1 ($\mathrm{NR\text{-}PM}_1$), from HR-ToF-AMS – **(F)** Toluene to benzene ratio, in downtown Paris (HS-PTRMS) – **(G)** absorption Ångström exponent as calculated using the aethalometer data.

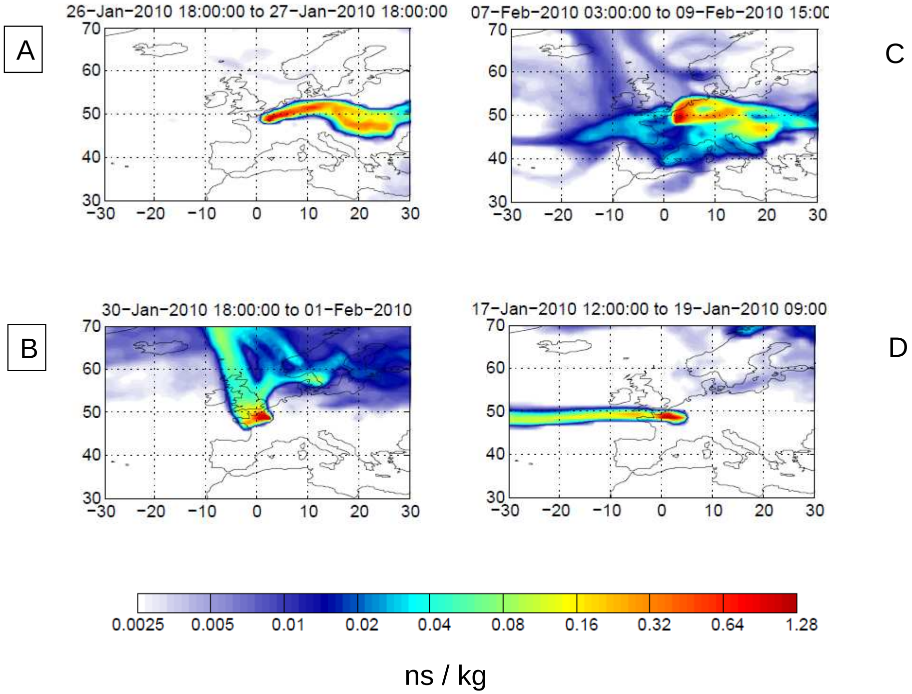

Fig. 4. Typical footprint potential emission sensitivities, from FLEXPART retroplume calculations. The X-axis represents the longitude while the Y-axis represents the latitude. Calculations are made for **(A)** and **(C)** the continental influence, **(B)** the biomass burning influence (SP2 coupled to HTDMA in this case), **(D)** the aged aerosol influenced air mass.

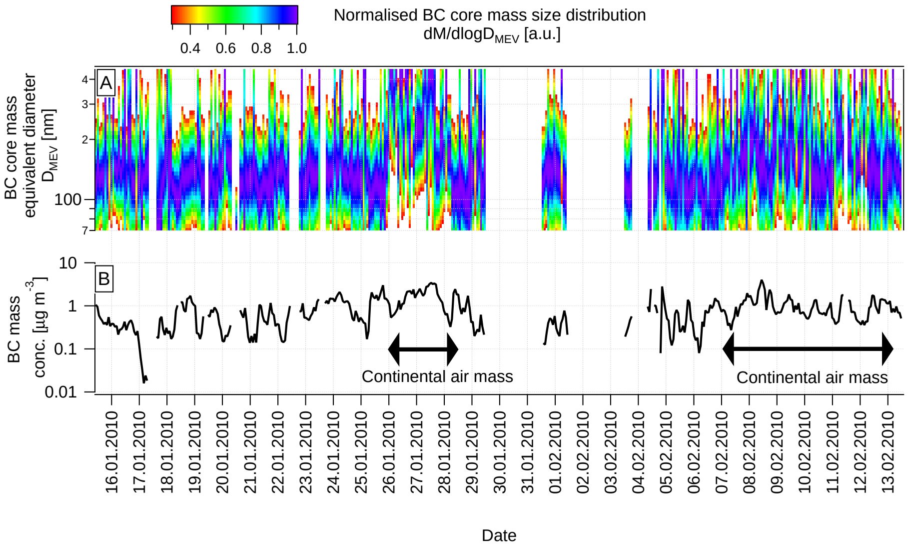

Fig. 5. (A) BC mass size distribution (normalised to its maximum) as a function of the BC core mass equivalent diameter, D_{MEV}, as measured by the SP2. **(B)** BC mass concentration as measured by the SP2.

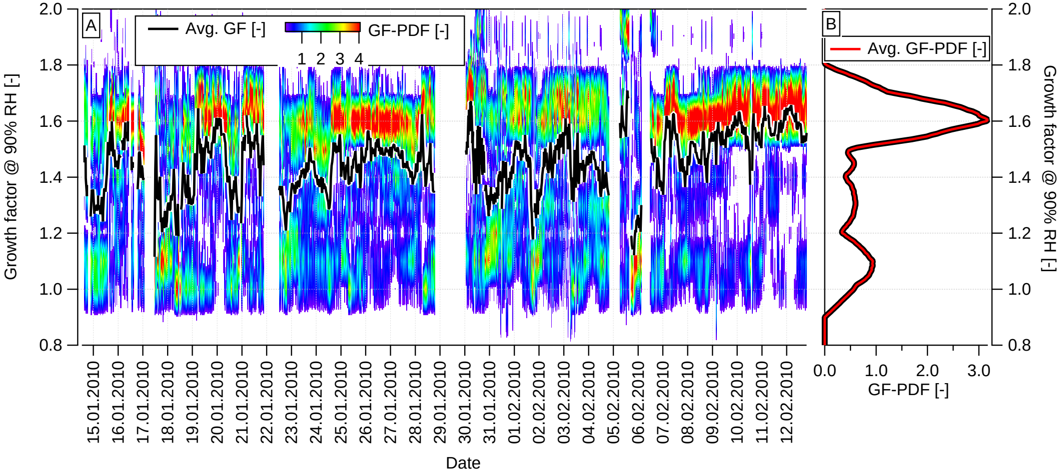

Fig. 6. (A) Growth factor probability distribution function (GF-PDF; contour plot) and average growth factor (black line) as measured by the HTDMA, at 90 % RH and for particles with a dry mobility diameter of D_0 265 nm dry mobility diameter. **(B)** GF-PDF averaged over the entire measurement period.

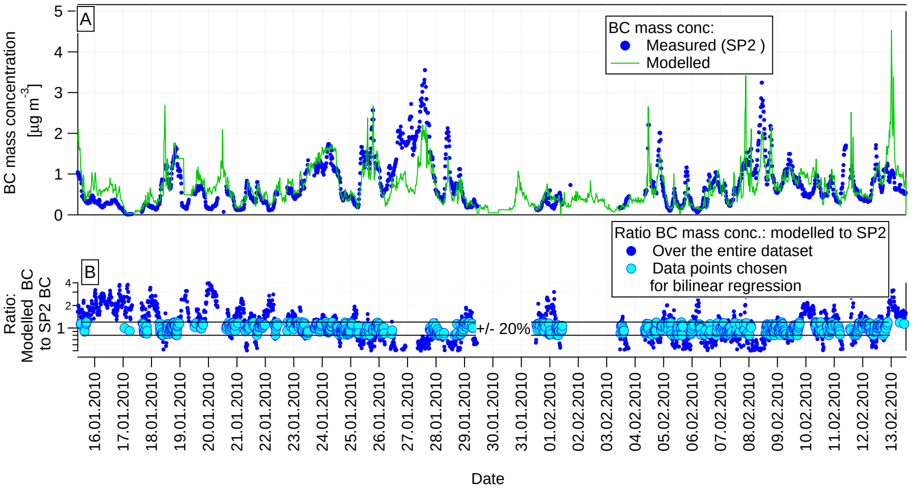

Fig. 7. **(A)** BC mass concentration, as measured by the SP2 and modelled with a bilinear regression. **(B)** Relative difference between modelled and measured BC mass concentrations. Only those data points for which the modelled BC mass concentration agreed within ±20 % with the measured BC mass concentration were considered for the bilinear regression.

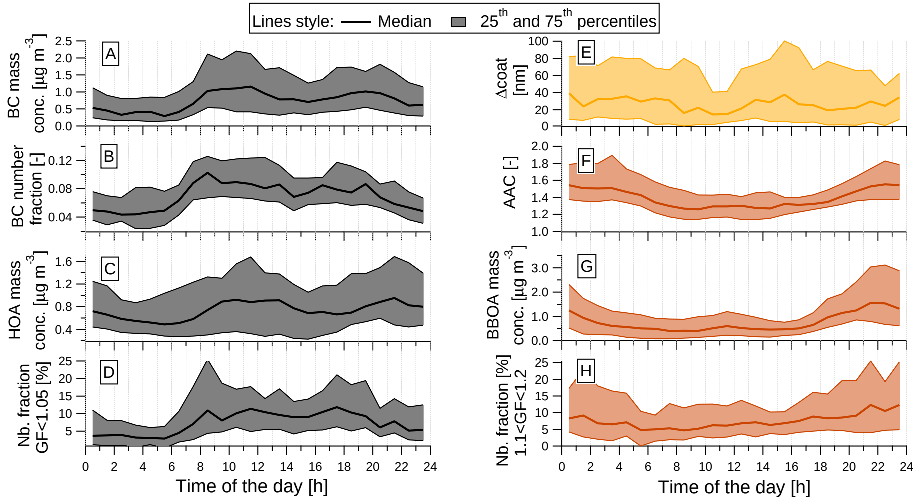

Fig. 8. Diurnal cycles of median, 25th and 75th percentiles of: **(A)** the BC mass concentration (SP2); **(B)** the relative number fraction of BC-containing particles (SP2) to the total number of particles (CN; measured by the SMPS); **(C)** the HOA mass concentration as retrieved from the HR-ToF-AMS measurement; **(D)** the number fraction of non-hygroscopic particles with GF $\leq$ 1.05 (HTDMA at 90 % RH); **(E)** the coating thickness of non-refractory matter on BC cores with a D_{MEV} between 180–220 nm (SP2); **(F)** the absorption Ångström exponent (calculated from the aethalometer data using Eq. 6); **(G)** the BBOA mass concentration as retrieved from the HR-ToF-AMS measurement; **(H)** the number fraction of slightly hygroscopic particles with 1.1 $\leq$ GF $\leq$ 1.2 (HTDMA at 90 % RH).

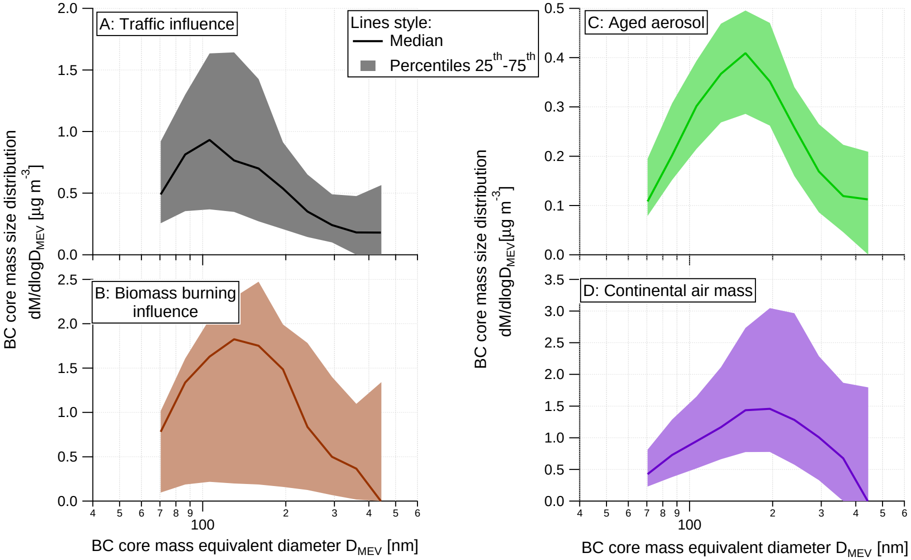

Fig. 9. Median, and 25th and 75th percentiles of BC core mass size distribution (SP2) for each air mass type.

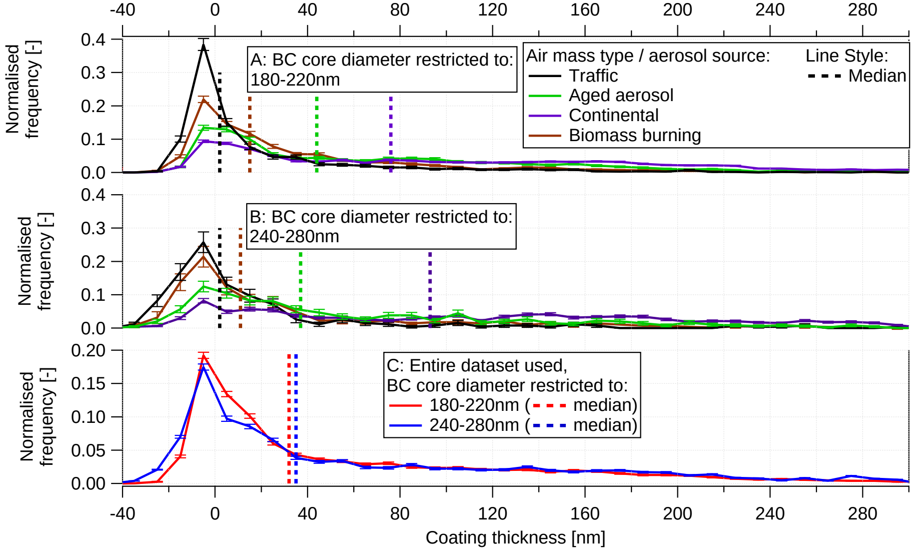

Fig. 10. Histogram (normalised by the area) of non-refractory matter coating thickness (Δ_{coat}) of BC cores with a D_{MEV} between 180–220 nm **(A)** and 240–280 nm **(B)**, for different air mass types /aerosol sources. Normalised histogram of Δ_{coat} for the entire dataset **(C)**. The error bars represent the statistical significance ($1/\sqrt{\text{number of points}}$).

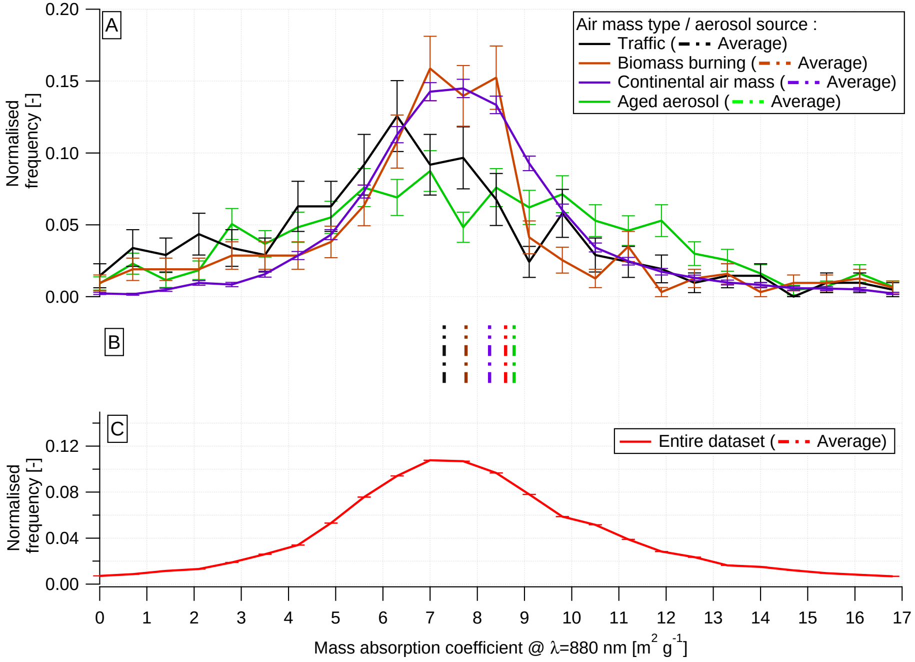

Fig. 11. Histogram (normalised to the area) of the mass absorption coefficients (MAC) for each air mass type/aerosol source **(A)** and calculated over the entire dataset **(C)**. Average MAC values corresponding to the histograms are shown in panel B. The MAC values were obtained using Eq. (6). The error bars represent the statistical significance ($1/\sqrt{\text{number of points}}$).

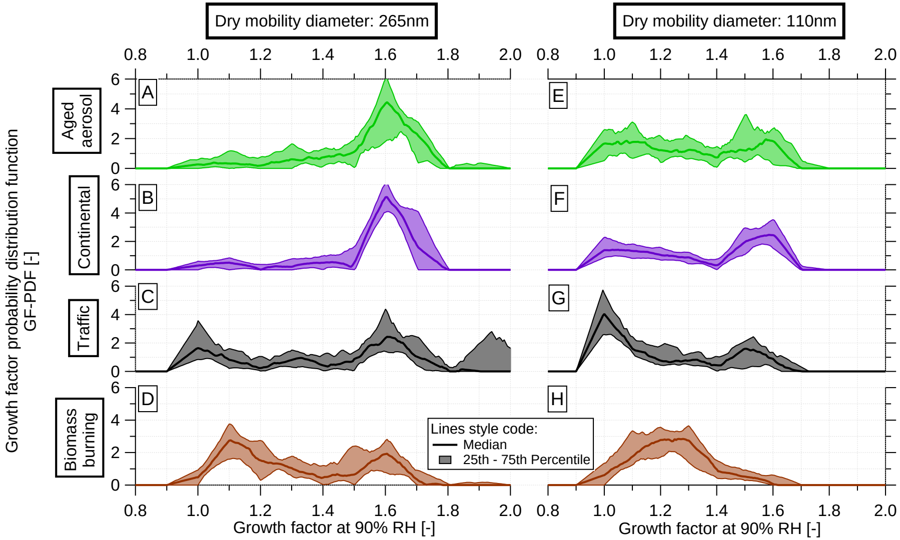

Fig. 12. Median (thicker lines) as well as 25th and 75th percentiles (thin lines and shading) of GF-PDF at RH = 90 %, for each air mass type/aerosol source and for two dry particle mobility diameters: 265 nm (left panels) and 110 nm (right panels).

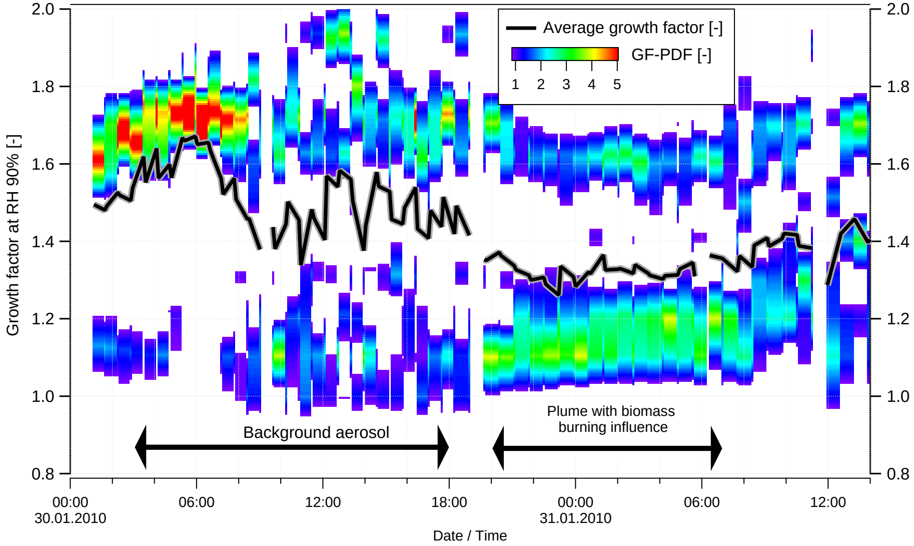

Fig. 13. GF-PDF at 90 % RH and D_0 = 265 nm during the period when the coupled HTDMA-SP2 setup was used. Two distinct periods with dominant influence from background aerosol and biomass burning are indicated by the black arrows.

Title Page
Abstract | Introduction
Conclusions | References
Tables | Figures
◀| | |▶
◀ | ▶
Back | Close
Full Screen / Esc
Printer-friendly Version
Interactive Discussion

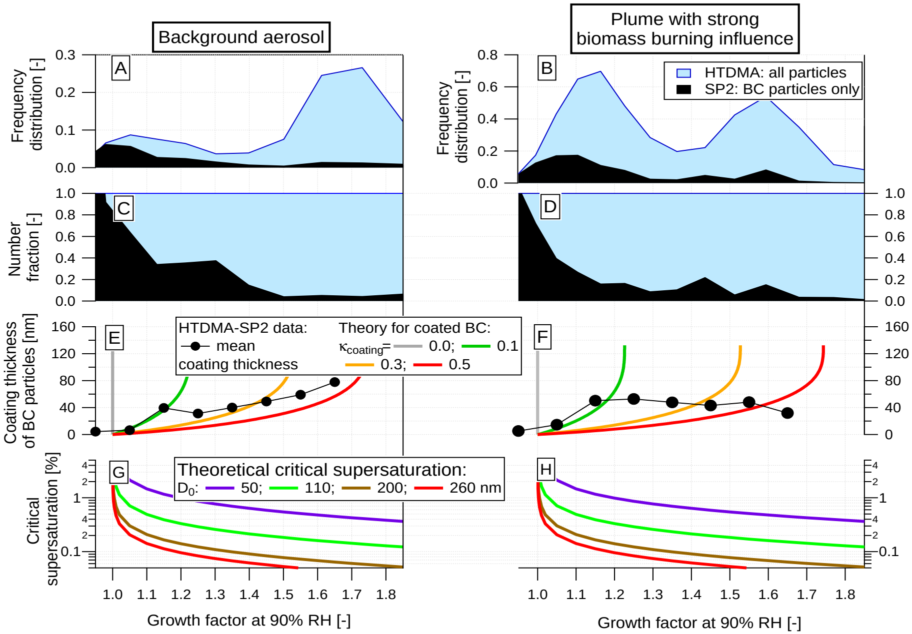

Fig. 14. Growth factor resolved properties of particles with a dry mobility diameter of D_0 = 265 nm obtained during the coupled HTDMA-SP2 setup for background (left panels) dominated and biomass burning dominated (right panels) periods. Measured GF-PDF at 90 % RH (**A** and **B**) for all particles (blue shading) and BC-containing particles (black shading). Number fraction of particles (**C** and **D**) with a BC core (black shading) and without a BC core (blue shading). Mean coating thickness of non-refractory matter on the BC cores (black circles; **E** and **F**). Theoretical GF as a function of coating thickness (**E** and **F**) for coating made of hydrophobic material (grey line), oxidized organics (green line), mixed organic/inorganic (yellow line) and sulphate (red line). Theoretical critical supersaturations necessary for CCN activation, as a function of growth factor and dry diameters (colour code in **G** and **H**).